



RESEARCH ARTICLE

10.1029/2018GC008085

Special Section:

Magmatic and volcanic processes in continental rifts

Key Points:

- Using high-resolution DEMs, we compare structures of four peralkaline rift volcanoes in Ethiopia and map previously unidentified post-caldera deposits
- Vent and crater locations and caldera architecture are controlled by both rift-parallel and cross-rift structures at each center
- Deposit volumes at each center and the rheology of peralkaline rhyolite coulees are estimated from morphometry

Supporting Information:

- Supporting Information S1

Correspondence to:

J. A. Hunt,
jonathan.hunt@earth.ox.ac.uk

Citation:

Hunt, J. A., Pyle, D. M., & Mather, T. A. (2019). The geomorphology, structure, and lava flow dynamics of peralkaline rift volcanoes from high-resolution digital elevation models. *Geochemistry, Geophysics, Geosystems*, 20, 1508–1538. <https://doi.org/10.1029/2018GC008085>

Received 20 NOV 2018

Accepted 9 FEB 2019

Accepted article online 21 FEB 2019

Published online 21 MAR 2019

The copyright line for this article was changed on 9 MAY 2019 after original online publication.

©2019. The Authors.

This is an open access article under the terms of the Creative Commons Attribution License, which permits use, distribution and reproduction in any medium, provided the original work is properly cited.

The Geomorphology, Structure, and Lava Flow Dynamics of Peralkaline Rift Volcanoes From High-Resolution Digital Elevation Models

Jonathan A. Hunt¹ , David M. Pyle¹ , and Tamsin A. Mather¹

¹COMET, Department of Earth Sciences, University of Oxford, Oxford, UK

Abstract Detailed topographic data from volcanoes can yield key insights into the controls on volcanic activity as well as hazards. High-resolution digital elevation models generated from remote sensing data enable comparison of the geomorphology and structure of large and inaccessible volcanoes. We present new topographic data for three peralkaline volcanoes in the Main Ethiopian Rift (Fentale, Corbetti, and Gedemsa) and one volcano in the Afar Rift (Dabbahu), combined with field observations, reveal previously unidentified post-caldera deposits and craters. Vent and crater locations are aligned with rift-parallel faults and also with rift-cutting structures in a variety of orientations. Caldera shape is controlled by interaction with these structures. The relative frequency and type of eruption varies greatly between these volcanoes over the past 150 kyr. Gedemsa is now largely inactive; Fentale hosts deposits from many small volume eruptions ($<0.1 \text{ km}^3$); while Corbetti has produced several large eruptions ($\sim 0.4\text{--}0.5 \text{ km}^3$). Morphometry of peralkaline rhyolite deposits at Corbetti and Fentale, including ogives and levees, provides constraints on rheology. Emplacement viscosities of $\sim 10^8\text{--}10^{11} \text{ Pa s}$ at Fentale are similar to or lower than calc-alkaline rhyolites and consistent with experimental and theoretical studies. The observations presented here have significant implications for hazard assessment in the Ethiopian rift and highlight the importance of structural features in controlling the location, magnitude, and style of volcanic activity in the Main Ethiopian Rift.

Plain Language Summary We created high-resolution topographic maps using images captured from space, or from aircraft, to investigate four Ethiopian volcanoes, which are large and in some cases inaccessible presenting challenges to studying them. These volcanoes are located in the Great Rift Valley, where the continent of Africa is splitting in two. We have identified deposits from previous eruptions, calculating their size and comparing typical eruptions for each volcano. At some volcanoes, the locations for each eruption line up parallel to fractures in the Earth's surface. In other places, locations line up with older faults that are now buried. The shapes of large craters have also been controlled by faults. The shapes of cooled lava flows suggest that the lava at Fentale may have been more fluid than typical lavas, owing to the unusual composition of lava found at rifts. Our study highlights key questions about volcanoes in rifts. We provide important observations for the assessment of future hazards at each volcano, located among a growing population and vulnerable infrastructure.

1. Introduction

The geomorphology of volcanoes has long been used to investigate volcanic development and activity (Thouret, 1999). Digital topography has been used to classify volcano morphology (e.g., Euillades et al., 2013; Favalli et al., 1999; Grosse et al., 2014; Pedersen & Grosse, 2014; Prima & Yoshida, 2010), identify and assess eruptive deposits and structures (e.g., Csatho et al., 2008; Hofton et al., 2006; Hutchison et al., 2015; Zouzias et al., 2011), and evaluate ongoing volcanic hazards (e.g., Favalli et al., 2005; Córdoba et al., 2015; Stefanescu et al., 2012). Many studies have used the morphometry of lava flow deposits (e.g., Nomikou et al., 2014; Pyle & Elliott, 2006; Tarquini et al., 2012; Ventura & Vilardo, 2007), cones (e.g., Fornaciai et al., 2012; Kervyn et al., 2012), and other deposits (e.g., Jessop et al., 2012) to investigate their rheology and dynamics of emplacement. The spatial distribution of vents, and orientations of craters and faults, can be used to investigate the influence of stress regimes and pre-existing structures on eruptive locations (e.g., Hutchison et al., 2015) and inform hazard assessment on the basis of likely event location. As satellite capabilities continue to develop, high-resolution remote

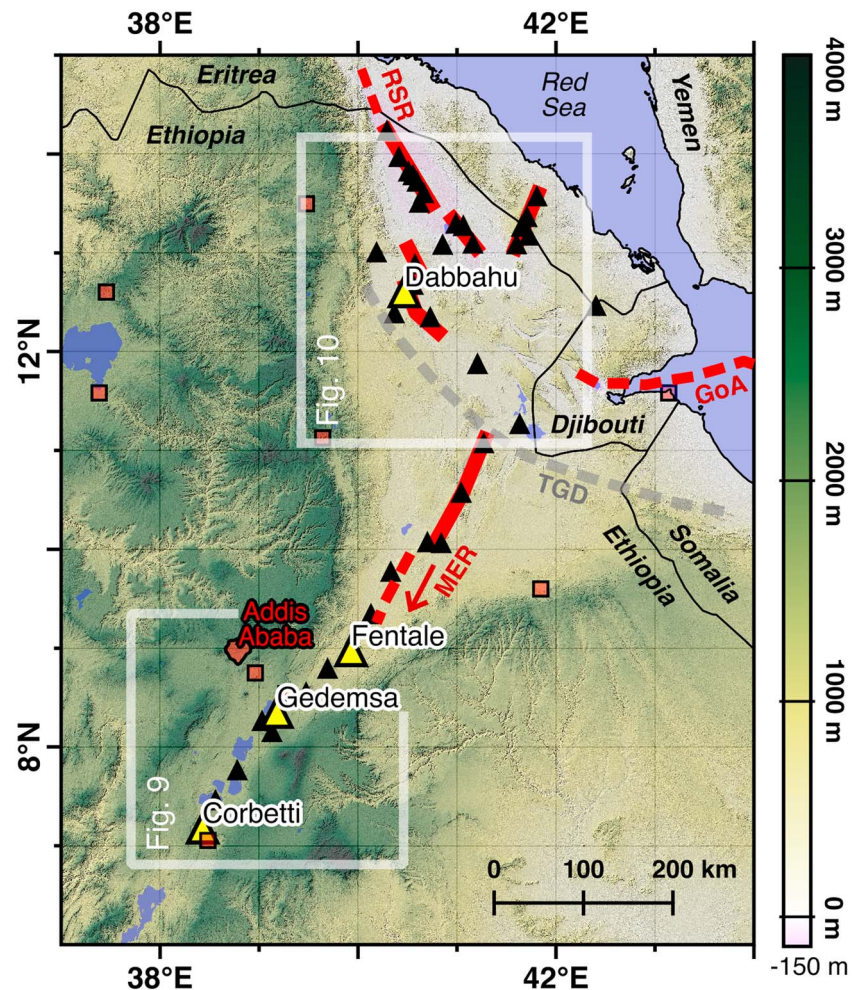


Figure 1. Location map for the volcanoes in this study (yellow triangles: Dabbahu, Fentale, Gedemsa, Corbetti). Elevation and hillshade provided by Aster Global Digital Elevation Model (product of METI and NASA). Shown in red dashed lines are the approximate locations of the three rifts that meet at the Afar triple junction: the RSR, GoA, and MER. Full red lines show rift segments in Afar (after Donovan et al., 2018; Wright et al., 2012). Gray dotted line delineates the TGD. Black triangles, other volcanoes; red squares, towns of population >100,000; black lines, country borders (Ethiopia, Eritrea, Djibouti, Somalia). RSR = Red Sea Rift; GoA = Gulf of Aden; MER = Main Ethiopian Rift; TGD = Tendaho-Goba Discontinuity.

sensing data are becoming increasingly important in studying large, inaccessible, and/or remote volcanoes across the world (e.g., Ernst et al., 2008; Favalli & Fornaciai, 2017; Kervyn et al., 2007).

Here, we demonstrate the use of high quality topographic data to develop and test hypotheses fundamental to rift volcanism and its dynamics. We use high-resolution digital elevation models (DEMs) to study the morphology of three volcanoes from the Main Ethiopian Rift (MER; Fentale, Gedemsa, and Corbetti) and one from Afar (Dabbahu, Figure 1). Using these data and complementary fieldwork, we (i) assess volcanic features, including observation of previously unidentified deposits; (ii) evaluate and compare caldera architecture; (iii) identify alignments of volcanic vents and craters; (iv) estimate eruptive volumes and frequencies along the rift; and (v) assess morphometry of peralkaline lava deposits. Peralkaline lavas (molar $[\text{Na}_2\text{O} + \text{K}_2\text{O}] / \text{Al}_2\text{O}_3 > 1$) with high alkali, halogen, and water content are common in rift settings (e.g., at Fentale; Webster et al., 1993). Experimental and theoretical studies suggest that such magmas have anomalously low viscosity due to depolymerization (e.g., Dingwell et al., 1998; Hess et al., 1995). No silicic peralkaline eruption has yet been observed, so the rheological constraints provided by morphology of peralkaline lava flow deposits are of significant interest and we further use our new data to assess the rheological properties of such flows.

1.1. Introduction to Volcanism in Ethiopia

Rifting in Ethiopia began in the Oligocene along the Red Sea Rift in Afar (~28 Ma; Wolfenden et al., 2005) and in the Miocene along the MER (~15–18 Ma; Wolfenden et al., 2004). Extension began along border faults, before migrating closer to the rift axis. The Red Sea Rift is more evolved than the MER, representing incipient seafloor spreading (e.g., Hayward & Ebinger, 1996; Keir et al., 2013). Continental rifting in the MER is more evolved in the north than in the south (e.g., Corti, 2009; Keir et al., 2015). The differences in maturity between and along rifts may lead to differences in present-day volcanic activity at within each rift.

Volcanic activity in the MER has formed both silicic peralkaline “central” volcanoes and distributed mafic cones and lavas (e.g., B. Abebe et al., 2007; Gibson, 1969). The poorly known volcanoes of the MER have become the focus of much recent work (Aspinall et al., 2011; Fontijn et al., 2018; Hutchison et al., 2015, Hutchison, Fusillo, et al., 2016, Hutchison, Biggs, et al., 2016, Hutchison, Pyle, et al., 2016, Hutchison et al., 2018; Lloyd, Biggs, Wilks, et al., 2018, Lloyd, Biggs, Birhanu, et al., 2018; Martin-Jones et al., 2017; McNamara et al., 2018; Rappich et al., 2016; Siegburg et al., 2017; Tadesse et al., 2018; Vye-Brown et al., 2016).

Previous work on the volcanoes in this study is summarized in Table 1. The central volcanoes commonly host elliptical calderas (Acocella et al., 2002), possibly influenced by structures cross-cutting the rift (e.g., B. Abebe et al., 2007). Reactivation of pre-rift structures is inferred to have influenced the development of both the caldera and post-caldera products, notably at Fentale, Gedemsa, and Corbetti (Acocella et al., 2002; Lloyd, Biggs, Wilks, et al., 2018). At Corbetti, surface deformation, internal structures, and post-caldera vents and craters are all thought to be controlled by cross-cutting structures, associated with a major crustal lineament (e.g., Corti, Sani, et al., 2018; Gíslason et al., 2015; Lloyd, Biggs, Wilks, et al., 2018).

The silicic MER volcanoes are in a post-caldera stage of evolution (Hutchison, Fusillo, et al., 2016). Four volcanoes have shown recent geodetic unrest (Aluto, Corbetti, Bora and Haledebi), with some deformation associated with ongoing geothermal activity (Biggs et al., 2011; Hutchison et al., 2015, Hutchison, Biggs, et al., 2016; Lloyd, Biggs, Wilks, et al., 2018, Lloyd, Biggs, Birhanu, et al., 2018). Corbetti and Aluto are considered the most active volcanic centers in the rift, with deposits from explosive eruptions implying an eruptive flux of 0.01–0.1 km³ (magma)/kyr over the past 12 kyr (Fontijn et al., 2018). This flux has declined significantly since the mid-Pleistocene peak of caldera-forming activity, when eruptive rates at Aluto and Corbetti may have been as high as 0.5–0.75 km³/kyr (Hutchison, Fusillo, et al., 2016).

The Afar region hosts a series of en-echelon magmatic segments analogous to seafloor spreading segments (e.g., Dabbahu/Manda Hararo, Alayta, Tat 'Ale, Erta 'Ale; Hayward & Ebinger, 1996; Keir et al., 2009; Wright et al., 2006, 2012; Figure 1) In comparison to the MER, volcanoes in Afar have been more active, with four eruptions in the period 2002–2015: Nabro, Alu-Dalafilla, Erta Ale, Dabbahu-Manda Hararo (Field et al., 2012; Field et al., 2013; Wadge et al., 2016). See Table 1 for further details of previous activity at Dabbahu.

2. Methodology

Very-high-resolution panchromatic (50 cm) and multispectral (2 m) orthoimages from the Pléiades-HR 1A satellite were obtained in stereo for three areas: Fentale, Gedemsa, and Urji (western half of Corbetti Caldera). In addition to the satellite-derived DEMs, lidar-derived DEMs of Chabbi (eastern half of Corbetti Caldera), and Dabbahu (Afar) are used in this study. The Urji and Chabbi DEMs were combined to create a merged DEM of Corbetti Caldera.

The satellite data were processed using the Leica Photogrammetry Suite; the full methodology is detailed by Zhou et al. (2015). The use of stereo images to create a DEM works on the principle of parallax. Two images from different perspectives can be joined together with tie points—the same feature identifiable in both orthoimages. Initial creation of a DEM using tie points results in a point cloud with a variable spatial density. Pleiades-derived DEMs have an average horizontal resolution of 1–2 m, varying with point cloud density due to lack/abundance of features and cloud cover. For analysis, it is convenient to regrid points using a block mean filter and an interpolation algorithm using continuous curvature splines, creating a regular grid of elevation values at 0.5-m spacing. Dense cloud cover must be removed from the point cloud. Cloud cover affects <8% of the stereo images for Fentale and is negligible for Gedemsa and Urji. Gaps in the final DEMs have been replaced by a low resolution model (30-m Aster Global DEM). Once a final point cloud is generated,

Table 1
Summary of Relevant Previous Work on Each Volcano in This Study

Volcano	Geology	Caldera	Post-caldera activity	Notable features	Dates
Fentale ^{a-d}	Major locations of eruptive activity: W, SE, and E of caldera. Edifice comprises trachytes and water-rich pantellerites with rare intercalated tuffs. ^{d,e}	Simple, regular ellipse with steep cliff. Long axis 273°. ^f	Several obsidian lava flows, within caldera and on NE flank. ^c Vents lie along fracture zone across caldera parallel to long axis. Historical basaltic volcanism, prior to ~1808–1810 CE, ^{g,h} following rift-parallel trend associated with tensional fissures. ^{a,i}	Fentale ignimbrite: associated with caldera formation. Forms thick deposit of welded ignimbrite on plain around edifice. Deposit is absent from much of the upper edifice. ^c Enigmatic blisters S of edifice may have formed by release of volatiles after emplacement. ^c	Fentale ignimbrite: 168 ± 38 ka (fission track dating on glass ^b).
Gedemsa ^j	Oldest products: pantelleritic lavas, followed by layers of pumice and dilute PDC deposits. ^h Two ignimbrites followed by further pumice deposits. ^{h,j}	Broad (~7 × 9 km) and low (max. topography ~100–150 m). ^f	Intra-caldera deposits follow a 280° trend. Three coalesced domes (Kelo, Dima and Kore) of lapilli and bomb breccias, interbedded with welded facies and obsidian lavas. ^h Kore hosts summit crater of ca. 600 m diameter. Ash-rich scoria cone and basaltic lava (NE rim of caldera) ^j related to regional faults. ^k	Pantellerite lava domes and pumice deposits outside caldera wall lie along extension ^f of post-caldera trend, ^f as well as along rift-parallel faults. ^j Age of these deposits is unknown.	Caldera: mid-Pleistocene, pre- and post-caldera deposits dated at 319 ± 2 ka and 265 ± 2 ka, respectively (K/Ar dates ^k).
Corbetti ^{l-m}	Three post-caldera edifices: Artu (oldest, partially buried ⁿ), Urji (syn. Wendo Koshe), Chabbi. Early post-caldera rocks are comenditic, shifting to pantelleritic in later stages. ⁿ	Old, large ignimbrites (0.9 and 0.67 Ma) suggest multiple caldera-forming eruptions. ^{n-p}	Urji comprises predominantly pyroclastic deposits, Chabbi predominantly obsidian lavas. Numerous craters on both Urji and Chabbi edifices, as well as a pumice flow on the N flank of Urji and six aphyric obsidian coulees on Chabbi. ^{n,q} Tephrostratigraphy suggests large explosive eruption every 900 years for the past 10 kyr. ^r	Most recent eruption from Urji emplaced Wendo Koshe Younger Pumice (WKYP), with four Chabbi lava coulees post-dating that event. ⁿ Post-caldera vents and craters are preferentially aligned to a cross-cutting structure. ^s Seismicity suggests the structure extends outside the caldera.	Ignimbrite: 182 ± 28 ka; post-caldera lava (E Chabbi): 19 ± 15 ka (both Ar-Ar) after hiatus. ^t WKYP: 2.3 ka (¹⁴ C, palaeosol ⁿ)

Table 1 (continued)

Volcano	Geology	Caldera	Post-caldera activity	Notable features	Dates
Dabbahu ^{u-v}	Basaltic trachy-andesites are common. Rhyolites divided into comendites, (summit and satellite centers), and pantellerites (series of N-S fissures).	Pit craters and/or small calderas at summit, elliptical structures to W.	Satellite centers of Alcoma, Gab'ho and Da'Ure. 3He dating of basalt surfaces indicates cyclic behavior (20–40 kyr periodicity). ^w The rifting episode of 2005–2006 resulted in a small eruption to S of Da'Ure (N-S trending vent and fault system deposited pumice ^x), followed by basaltic eruptions further south. ^y	Elliptical structures associated with fumaroles identified. ^u Summit craters smaller than MER calderas. Larger structures may have been buried. Extensive suite of lavas from basalt to peralkaline rhyolite, in contrast to MER where intermediate compositions largely absent.	

Note. PDC = pyroclastic density current.

^aGibson (1967). ^bGibson (1969). ^cGibson (1970). ^dGibson (1974). ^eWebster et al. (1993). ^fAcocella et al. (2002). ^gHarris (1844). ^hFontijn et al. (2018). ⁱWilliams et al. (2004). ^jThrall et al. (1973). ^kPeccerillo et al. (2003). ^lMohr (1966). ^mDi Paola (1971). ⁿRappich et al. (2016). ^oŽáček et al. (2014). ^pŽáček et al. (2015). ^qMacdonald and Gibson (1969). ^rMartin-Jones et al. (2017). ^sLloyd, Biggs, Wilks, et al. (2018). ^tHutchison, Fusillo, et al. (2016). ^uField et al. (2013). ^vField et al. (2013). ^wMedynski et al. (2013). ^xWright et al. (2006). ^yFerguson et al. (2010).

raster images of elevation are created and images of hillshade and slope can be calculated. The lower resolution multispectral images were pansharpened using the 50-cm resolution panchromatic images and used for feature identification and mapping.

Lidar data were acquired by the U.K. Natural Environmental Research Council's Airborne Research and Survey Facility in October 2009 (Dabbahu) and November 2012 (Chabbi). A DEM of 0.5-m pixel resolution was generated for Dabbahu by Barnie et al. (2016); full details of processing are provided in Hofmann (2013). A DEM of 2-m resolution was generated for Chabbi using Geographic Resources Analysis Support System (<http://grass.osgeo.org/>) as described in Hutchison et al. (2015).

From these models and using QGIS (<http://www.qgis.org>), we manually mapped vents, craters, faults, cones, flow deposits, and other features at each volcano. We used a scale of 1:5000 in identifying features and a scale of 1:2500 in drawing contacts. Rose diagrams were then produced for craters, faults, and other linear features observed from the DEMs, weighted by length. Vent/crater alignments were manually identified on the basis three or more features and/or elongation of craters/cones.

Due to the lack of recent studies at Fentale and its complex geomorphology, we conducted a 1-week field campaign in November 2017 to complement DEM observations and ground truth results relating to flow deposits and relations between units. Access to the north and east of the edifice is restricted, while the steep slopes of the volcano prevent detailed exploration of many other areas. The high-resolution DEM provided an invaluable base map for making field observations and enables us to apply these observations more generally. The campaign was in part targeted, prioritizing geomorphological features such as levees identified from the DEM, and in part exploratory, surveying the accessible southern flank of the volcano.

Volumes of features such as lava flow deposits and cones were estimated using a DEM-differencing technique: A feature is masked and the resultant gap in the data is interpolated using the same surface gridding algorithm (continuous curvature splines) used in the original DEM construction. A similar method was used to estimate lava flow deposit volumes on the Kameni islands, Santorini, by Nomikou et al. (2014). A variable tension factor (between 0 and 1) is used during interpolation to find the pre-eruptive surface—we found that a factor of 0.7 produced geologically reasonable surfaces, with little dependence on tension above a factor of 0.3. For the Kameni islands, minimum and maximum volumes were calculated for lava flow deposits, varying by <25% (Nomikou et al., 2014)—we follow Hutchison, Pyle, et al. (2016) in using this value as an approximation of error using this method.

A number of studies have used morphometry to estimate the rheology of lava flow deposits (e.g., Fink & Griffiths, 1990; Gregg, 2017; Gregg & Fink, 2000; Hulme, 1974; Moore et al., 1978; Nomikou et al., 2014; Pyle & Elliott, 2006; Wadge & Lopes, 1991; Wilson & Mouginis-Mark, 2014). Assuming a constant Bingham rheology, the apparent yield strength of a fluid can be estimated from the dimensions of the deposit (Gregg, 2017; Hulme, 1974). For a deposit of thickness, h ,

bulk density, ρ , emplaced on a slope of angle, α , the yield strength, Y , is

$$Y = h g \rho \sin \alpha. \quad (1)$$

Coulees on both Corbetti and Fentale exhibit surface wrinkles, or ogives. Frequency analysis of elevation data along profiles down the length of the coulee can provide a quantitative assessment of the wavelengths of these features (Lescinsky et al., 2007; Pyle & Elliott, 2006), which depends on the viscosity of the lava and the thickness of the solidifying crust (Fink & Fletcher, 1978; Warner & Gregg, 2003). Using custom scripts in MATLAB, data from the profiles were filtered with a band-pass filter (5–100 m) and Fast Fourier Transform analysis was performed along each profile within windows of length 200 m, with an overlap of 150 m.

Studies of rheology from levees/channelized flows have largely focused on basaltic lava (e.g., Cashman et al., 2013; Mazzarini et al., 2005; Wantim et al., 2013). Kerr et al. (2006) considered the channelized flow of lava on an unconfined slope. They suggest an initial phase of both down-slope and across-slope flow before a later phase of constant width. Lateral spreading is limited by the growth of a cooling crust on the surface of the flow (Deardorff & Cashman, 2012; Kerr et al., 2006—who consider a range in composition from basaltic andesite to dacite). The width of the flow channel, W , limited in this way depends on the angle of the slope, θ , according to

$$W = 2 \left[\frac{(g \Delta \rho)^2 Q^7 \mu^4 \cos^9 \theta}{\sigma^6 \kappa^3 \sin^7 \theta} \right]^{1/13}, \quad (2)$$

which can also be written

$$W = \Phi \left[\frac{\cos^9 \theta}{\sin^7 \theta} \right]^{1/13}, \quad (3)$$

where

$$\Phi = 2 \left[\frac{(g \Delta \rho)^2 Q^7 \mu^4}{\sigma^6 \kappa^3} \right]^{1/13}, \quad (4)$$

in which g is gravity (m/s^2), $\Delta \rho$ is the density difference between lava and air (kg/m^3), Q is the volumetric flow rate (m^3/s), μ is the viscosity of the lava (Pa s), σ is the effective yield strength of the crust (Pa), and κ is the thermal diffusivity of the lava (m^2/s). We present measurements of channel width versus angle of slope for coulees at Fentale to provide reasonable bounds for volumetric flow rate and emplacement viscosity.

3. Results

An overview of the main features of each volcano is presented in Table 2. Satellite imagery and DEMs of Fentale, Gedemsa, and Corbetti enable an assessment of geomorphology and geological units, some of which have been mapped previously. Here we compare these DEMs with previously observed features and make new observations of volcanic structures and deposits. In sections 4.1–4.4 we present results from each of the volcanoes in this study, including a longer section for Fentale owing to more newly identified features and additional detail from field observations. In section 3.5 we present results from flow morphometry.

In the absence of field observations for most of the study areas, we are unable to distinguish between some deposits formed by lava flows, pyroclastic density currents and other types of flows—we use the term “flow deposit” to describe these. For deposits identifiable as formed by silicic lava flows, we use the term “lava flow” during deposition and “coulee” after deposition.

3.1. Fentale

3.1.1. Large-Scale Observations

Fentale is a tall edifice with a narrow and deep caldera (Figure 2 and Table 2). The edifice footprint is comparable to other MER volcanoes, although burial of the lowest flanks obscures the full extent of Fentale's structure. In places, the low relief outlines of the buried edifice are exposed.

Table 2
Attributes of Each Volcano Edifice and Caldera in This Study

Volcano	Peak elevation, m	Height ^a , m	Area ^a , km ²	Caldera width, km		Caldera long-axis orientation	Caldera relief, m ^b
				Short axis	Long axis		
Fentale	1,940	980	140–200	2.9	4.4	112°N	150–400
Gedemsa	1,940	390	100–130	7.3	9.6	75°N	0–270
Corbetti	2,300	560	220–260	10.9	15.6	104°N	0–150
Dabbahu	1,360	940	180–450	-	-	-	-

^aHeight and area were estimated by drawing two polygons (minimum and maximum) around the edifice bounding the topographical footprint of each volcano. The area of the edifice was calculated, and the peak elevation minus the lowest elevation at the polygon limits provided an estimation of height. ^bAn estimate of caldera relief was calculated by subtracting the elevation of the caldera floor near the rim from the elevation at the top of the rim nearby. Minima and maxima are presented for each caldera.

The edifice flanks consist of shallow-sloped (~3–15°) lobate features bounded by steep slopes (Figure 2d). There are notable flat-topped ridges in the west (oriented E-W) and north (oriented N-S). The higher flanks are steeper, more variable in slope (~10–40°, Figure 2d) and host a much greater complexity of geomorphological features.

The lobate features with shallow/flat tops are interpreted as flow deposits of the Fentale ignimbrite and other pyroclastic material. The lack of burial by later deposits preserves the geomorphology of older overlapping deposits on the higher flanks.

Fentale's caldera is regular and elliptical, as observed by Acocella et al. (2002), although the northern rim of the caldera is straight and forms a linear feature trending ~291° (~WNW-ESE). This trend is in the same direction as the caldera long axis. The elevation of the caldera rim varies between 1,600 and 1,850 m (above sea level), with the highest cliffs to the west, to the north, and to the south-east. The elevation of the caldera infill ranges from ~1,450 m in the west to ~1,650 m in the east. The sharp edge of the crater bisects several preexisting morphological features. Along segments of the crater rim lacking these topographical highs, the rim is lower and more uniform in elevation (north, south-west, north-east). Field mapping shows that variably welded ignimbrite has been deposited in smaller valleys around the caldera (Figures 3 and 4b).

The areas of uniform rim elevation correspond to the major eruption pathways suggested by Gibson (1970). Our observations show that the deposits from the caldera-forming eruption are thickest in preexisting topographic lows. In the broad valleys between ridges on the south-western side of the edifice, ignimbrite deposition was particularly significant and is associated with distinctive, level topography and relatively even slopes. Surficial deposits at higher elevations may have been lost in later erosion.

Two ridges, aligned W and SSW, project from the caldera on the western side of the edifice (Figures 2c and 2d). A number of dome-shaped structures are clustered on the eastern side of the edifice, oriented approximately NNE-SSW, including the south-east center of Gibson (1967). The east and west centers are also apparent, in addition to minor domes at the bottom of the upper flank to the south. The tallest point on the edifice is the peak of a dome close to the eastern rim of the caldera.

3.1.2. Coulees

Young post-caldera obsidian coulees are observable from the topography and were mapped by Gibson (1967, 1974). The morphology of the coulees is strongly controlled by preexisting topography, forming narrow channels down steep valleys (e.g., south-eastern and south-western flanks; Figures 2a and 3). Field observations from the coulee on the south-eastern flank (SE, Figure 2a) show a crystallinity of ~10% and reveal the presence of crystal cumulates (Figures 4f and 4g). Coulees along the western ridge (W1-3, Figure 2a) are overlapped by the Fentale ignimbrite and are therefore pre-caldera.

The coulee on the north-eastern flank (NE, Figure 2a) exhibits flow wrinkles, or ogives, that form double chevrons due to the extended flow in two neighboring valleys. Levees are common in both pre- and post-caldera coulees, across the lower flanks of the edifice, and around the dome-shaped structures on the eastern flank. They range in width between 30 and 400 m. An obsidian coulee on the northwestside of the edifice (NW, Figure 2a) displays well-formed levees accompanied by a breakout structure as the channel is

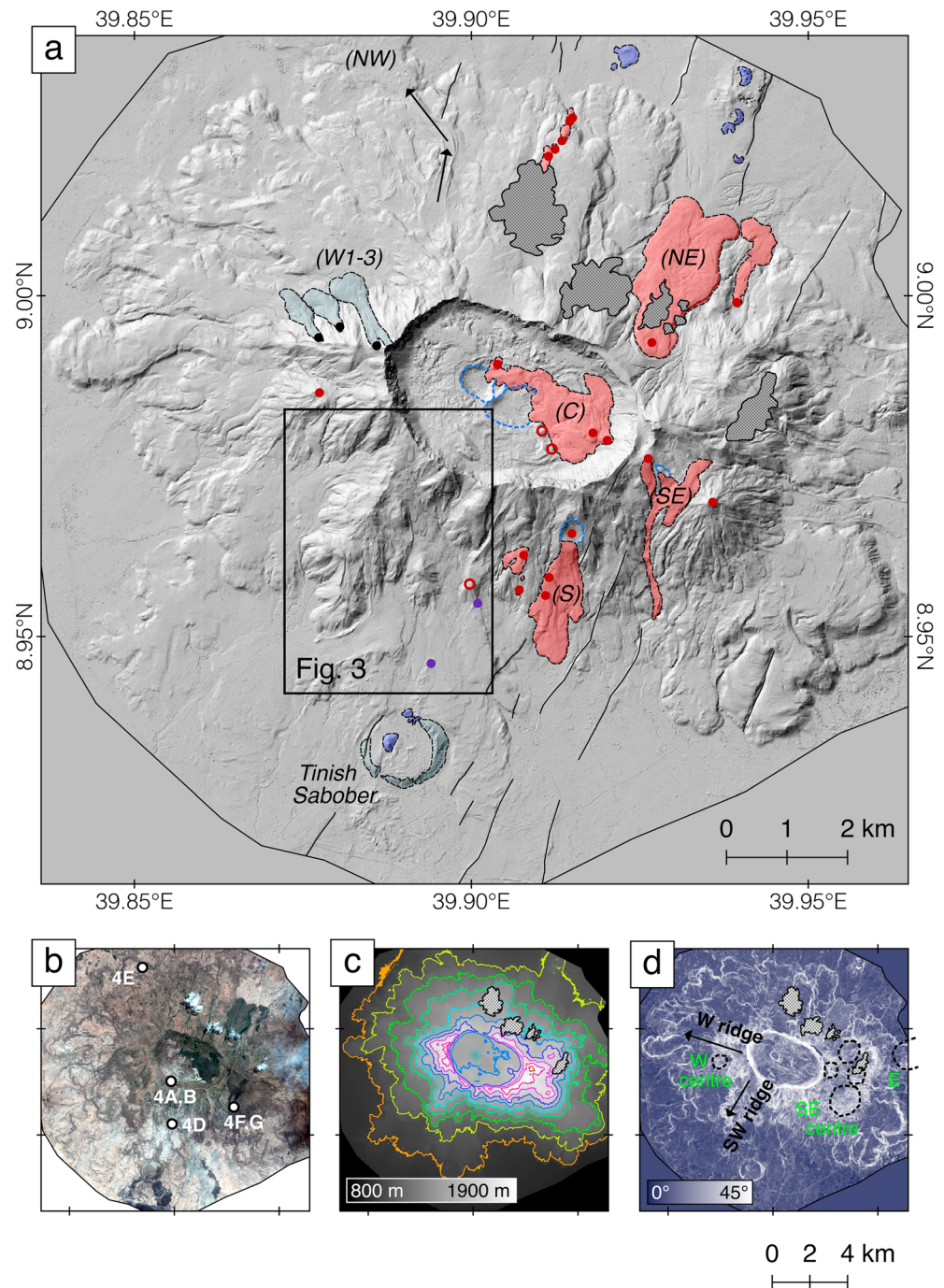


Figure 2. Maps derived from the digital elevation model of Fentale, clouds are masked in gray. (a) Hillshade map, illuminated from 300°N. Key features discussed in the text are highlighted, including post-caldera coulees (red), basaltic scoria cones (blue), other notable deposits (gray), craters (blue dashed line), faults (black line), and vents (post-caldera silicic, red; pre-caldera silicic, black). (b) Pansharpened multispectral image of Fentale, locations of photographs in Figure 3 are labeled. (c) Elevation map, with contour lines every 100 m. (d) Slope map, with key ridges and domes labeled.

deflected by $\sim 60^\circ$. The coulee fans out on the horizontal plain which surrounds the edifice, forming enigmatic ripple structures. Much of this coulee is covered by variably welded ignimbrite, as observed in the field (Figure 4e). The partial burial of pre-caldera lava coulees with ignimbrite is a common observation across the lower flanks of Fentale.

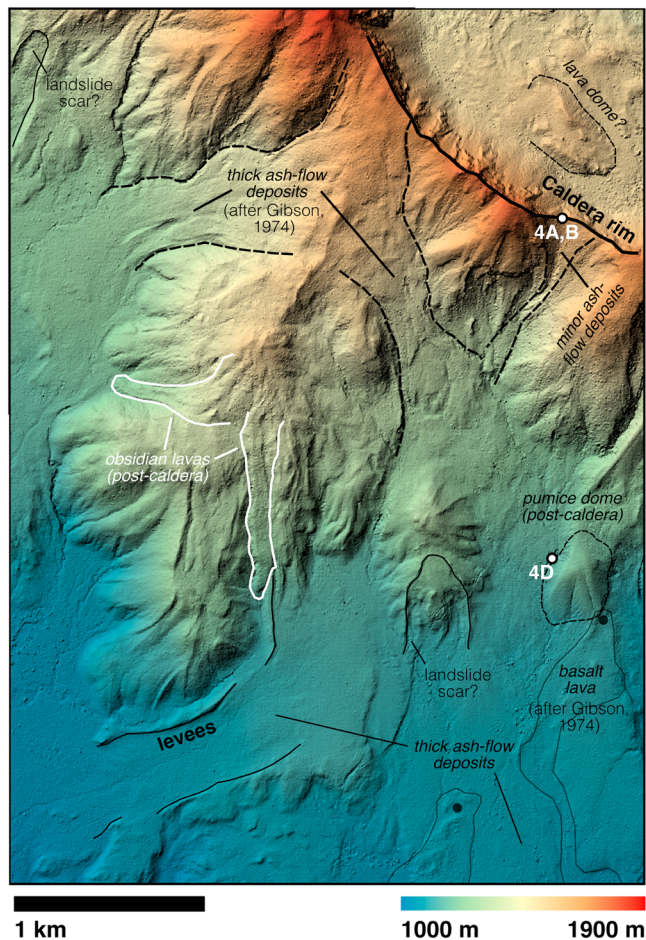


Figure 3. Combined hillshade and elevation map of the south-west ridge of Fentale, with features labeled. The limits of the basalt lava and thick ash deposits are after Gibson (1974), the rest of the features are newly identified in this study using a combination of field and digital elevation model observations (section 3.1.3).

Vents are identifiable from elevated points in the coulee, with multiple vents commonly feeding a single flow (Figure 2a). The lava coulees within the caldera and on the south-eastern flank (C and SE, Figure 2a) are fed by vents aligned in the WNW-ESE direction, a trend shared by the vents feeding individual pre-caldera flows along the western ridge (W1-3). The lava coulee on the southern flank (S) is fed by two-thirds vents aligned in the NNE-SSW direction, a trend common to nearby faults and fissures. The extension of this trend northward may intersect the vent for the coulee on the north-eastern flank (Figure 2a).

Several small volume features accompany the coulee on the southern flank (400×400 m), mapped as post-caldera obsidian lavas by Gibson (1967, 1974). Further features are identified on the northern flank which we propose as additional small lava coulees (150×300 m), though field observations are required for validation. Vent spacing ranges from 200 up to 2,000 m for the larger flows. Volumes have been calculated for the lava coulee within the caldera (C, 0.034 km^3) and for the coulees on the north-eastern (NE, 0.091 km^3) and southern flanks (S, 0.015 km^3 ; Table 3). Pre-caldera coulees on the western ridge are much smaller in volume ($0.003\text{--}0.004 \text{ km}^3$).

The coulees on the western ridge have lengths of ~ 1 km compared to 2–2.5 km for post-caldera coulees (Table 4 and Figure 2a). The larger pre-caldera coulees, evidenced by relict flow morphology now partially buried, have lengths up to and exceeding 5 km. The coulees on the western ridge (W1-3) have variable aspect ratios, starting low ($\sim 5\text{--}8$) and increasing away from the vent as the pre-eruptive slope shallows (ending $\sim 10\text{--}14$; Table 4). Coulees on the south-west ridge and the north-east slope end with a lower aspect ratio—we interpret this as the flow stopping prior to build up at the flow nose (Figures 2a and 3).

3.1.3. Additional Observations

A broad crater to the south of the edifice named Tinish Sabober was mapped as a tuff ring by Gibson (1967) and Williams et al. (2004; Figure 2a). The ring is buried in places by deposits including the

Fentale ignimbrite, suggesting that it predates the caldera-forming eruption. The surviving topography of the tuff ring provides a minimum volume estimate of 0.0054 km^3 (Table 3).

Two craters are nested in the center of the caldera, with areas of 0.2 and 0.05 km^2 . The larger crater is elongated in the WNW-ESE direction, similar to the caldera, whereas the smaller crater is elongated in the NNE-SSW direction, along the rim of the larger crater (Figure 2a). The craters precede the emplacement of the obsidian coulee. The presence of additional craters, cones, and domes, together with observations of surficial pumice, suggests multiple intra-caldera explosive and effusive eruptions (Figure 3 and Text S1).

There is a steep gorge down the caldera rim on its eastern side; we observed a column of steam rising from the base of this gorge, suggesting the presence of a hot spring or fumarole. We interpret the alignment of vents, a geothermal manifestation and a steep gorge as evidence of a fault striking \sim ESE.

Additional post-caldera deposits have also been observed on the flanks of the edifice. A pumice cone is located at the base of the southern upper flanks (Figure 3) and is associated with a fresh pumice deposit distributed across the nearby slopes. A new obsidian coulee was also observed along the south-west ridge, overlying the variably welded ignimbrite (Figure 3). Further post-caldera deposits may yet be unmapped on Fentale given the size and inaccessibility of the volcano—this remains a priority for further study. Concave structures have been identified as possible landslide scars in a number of locations (Figure 3), indicating the potential for collapse of unstable slopes on the flanks of the edifice.

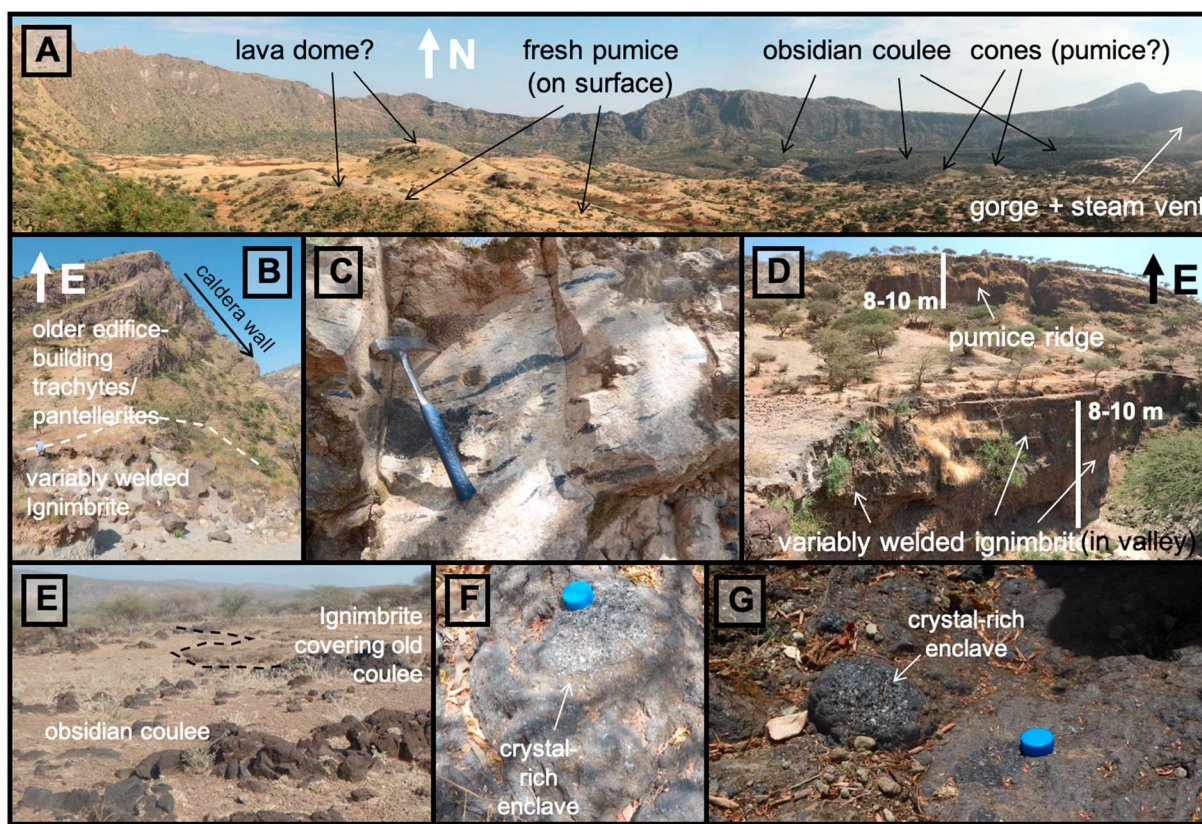


Figure 4. Field photographs from Fentale; locations are labeled in Figures 2, 3. (a) Panorama of caldera, including evidence of post-caldera eruptions. (b) Ignimbrite in small valley near the caldera rim (photograph taken from same location as (a)). (c) Example of fiamme within welded section of ignimbrite. (d) Pumice ridge and ignimbrite within a valley, southern flank of Fentale. (e) Example of ignimbrite partially covering the pre-caldera obsidian coulee, north-west Fentale. (f and g) Crystal-rich enclave in post-caldera obsidian coulee, south-east flank of Fentale.

The recent basaltic volcanism is visible on the satellite imagery (Figure 2b) but produces negligible topography. The vents are not easily identifiable but seem to have a strong association with rift-related faults/fissures and NNE-SSW trend, encroaching onto the edifice (Williams et al., 2004). The most northerly basaltic vent is located close to the pumice cone on the southern flank of the volcano (Figure 3).

Regional normal faults, striking ~NNE, intersect the edifice creating offsets of up to 10–15 m. Faults are particularly prevalent on the western side of the edifice, along with the majority of post-caldera eruptive vents (Figure 2a). Associated with regional normal faults, basaltic cones have been emplaced to the north and south of the edifice (Figure 2a, Text S1).

Blister structures hosted by the ignimbrite are particularly prevalent on the flat plain to the south, close to the present-day Lake Metehara. We mapped blisters across an area of 1.5 km² and found no systematic variation of size or orientation (Text S1 and Figures S1–S2). The low-lying ground could have been a source of groundwater which boiled after burial by ignimbrite, providing steam which expanded to form the blisters, in a manner analogous to the formation of rootless cones (Baloga et al., 2007; Fagents & Thordarson, 2007).

3.2. Gedemsa

The edifice of Gedemsa is broad and shallow and has been largely evacuated by caldera-forming eruptions (Figure 5 and Table 2). The remaining edifice forms a broken, arcuate structure with its highest elevations to the east (1,900 m) and south (1,950 m; Figure 5c). The pre-caldera edifice is the most extensive in the north-east, in the form of broad, fault-cut lobes, and in the south, with a ridge projecting southwards (Figure 5b and 5c).

A ridge to the west forms the limit of the edifice and the eastern limit of Lake Koka, striking NNE along a regional normal fault (Figure 5b). Two or three pantellerite domes/coulees with volumes of ~0.02–0.1 km³ form satellite centers up to 9 km from the center of the Gedemsa caldera. The significant fault which

Table 3

Volumes of Features on Each Volcano (see Figures for Locations: Figure 2a, Fentale; Figure 5a, Gedemsa; Figure 6a, Corbetti; and Figure S3 for Summary), With an Approximate Error of 25% (see Section 2; Hutchison, Pyle, et al., 2016; Nomikou et al., 2014)

Volcano	Feature	Volume, km ³	Area, km ²	Vol/area, m
Fentale	Total silicic post-caldera ^a	<1.0		
	Individual features			
	Dome ^b (W)	0.061	6.08	10
	Lava coulee (S)	0.015	3.84	3.8
	Lava coulee (NE)	0.091	9.72	9.4
	Lava coulee (C)	0.034	12.0	2.8
	Lava coulee (W1)	0.0038	1.84	2.1
	Lava coulee (W2)	0.0029	1.31	2.2
	Pumice cone	0.0036	1.33	2.7
Gedemsa	Tuff ring	0.0054	2.88	1.9
	Total silicic post-caldera ^a	<1.0		
	Individual features			
	Intra-caldera deposits	0.57	51.9	11
	Dome (E)	0.11	9.96	11
	Dome (SW)	0.11	7.37	15
	Dome (NW)	0.021	4.32	4.9
	Scoria cone (NE)	0.013	3.32	3.9
	Scoria cone (SE)	0.0061	2.49	2.4
Corbetti	Scoria cone (SW)	0.0043	2.33	1.9
	Scoria cone (W)	0.0039	1.48	2.6
	Total silicic post-caldera ^a	14.5		
	Individual features			
	Artu	0.61	48.7	12
	Urji	6.36	133	48
	Chabbi	7.53	169	45
	WKYP flow deposit	0.26	16.8	15
	Lava coulee (CO6)	0.47	40.5	12
	Tuff ring	0.038	9.72	3.9

^aEstimated by summing individual features for Fentale and Gedemsa and summing the Artu, Urji, and Chabbi for Corbetti. Additional post-caldera features may be unaccounted for at Fentale and Gedemsa. ^bDomes may be composite structures, formed of multiple events.

delineates the ridge also dissects a dome in the NW suggesting continuation of fault activity after dome emplacement (Figure 5b).

Numerous normal faults cut through the eastern side of the caldera with variable offsets both on the old edifice and on the caldera floor (Figure 5). Within the caldera the faults appear to splay into multiple fractures of smaller offset—we suggest that this is the result of lower cohesive strength of lake sediments in the shallow subsurface. These faults are not collocated with volcanic products but are apparently independent from the activity of Gedemsa volcano.

The caldera wall is heavily and variably eroded, and partially covered by later deposition of lake sediments. It hosts several embayments and arcuate features on its eastern end related to rift-related normal faults (Figure 5a). The northern and southern sections of the caldera are straight and parallel; we suggest this indicates a possible influence of cross-cutting structures striking ~ENE-WSW.

The elevation of the caldera floor ranges from ~1,570 m in the north to nearly 1,700 m in the south, immediately to the west of the regional normal faults (Figure 5c). The center of the Kore crater has an average elevation of ~1,620 m. The crater predates the dome that partially covers its north-east rim. The central domes vary in morphology from smooth and gentle topography to incised (Figure 5a). The westernmost of the three coalesced domes, Kelo, hosts a ridge striking NE-SW in line with a portion of the caldera wall to the NE. The ridge is highly incised by valleys in comparison to the two domes at each end of the ridge, perhaps suggesting an older age or softer material.

Additional areas of elevated relief are also observed within the caldera: A broad prominence is located in the northern half of the caldera, with three or four steeper hills in the south (Figures 5a and 5c). These may be related to activity postdating caldera formation but older than the formation of the Kore crater and related domes.

Table 4
Attributes of Lava Coulees on Fentale, Including Aspect Ratios at Successive Points Away From the Vent

Location	UTM of vent(s) (easting, northing)	Length, m	Aspect ratio			Width of levees, m	Average slope (channel), deg
			Width, m	Height, m	W/H		
Western ridge (W1)	4439129, 1005311	1,040	85	17	5.0	-	-
			135	17	7.9		
			328	44	7.5		
			240	28	8.6		
Western ridge (W2)	4439483, 1005474	970	113	17	6.6	-	-
			278	28	9.9		
			395	38	10.4		
			448	30	14.9		
Western ridge (W3)	4440089, 1005138 4440338, 1005122?	1,350	90	15	6.0	20–50	25.5
			142	18	7.9		
			510	40	12.8		
North-west	4441137, 1006918?	~5,000	533	32	16.7	60–140	5.4–7.0
			287	16 ^a	17.9 ^a		
			1,313	35 ^a	37.5 ^a		
			2,174	44 ^a	49.4 ^a		
SW ridge (see Figure 3)	4439917, 1002394?	>1,090	85	10	8.5	-	-
			85	12	7.1		
			121	12	10.1		
			113	18	6.3		
S slope (S)	4443244, 1001995 4442924, 1001366 4442885, 1001080	2,110	520	58 ^b	9.0 ^b	-	-
			563	24	23.5		
SE dome	4444570, 1003332 4445276, 1002800	2,520	134	11	12.2	30–70	11.9
			148	5	29.6		
Caldera (C)	4443637, 1003769 4443903, 1003637 4442444, 1004767? 4442090, 1004891?	2,340	717	30	23.9	-	-
			335	27	12.4		
NE slope (NE)	444656, 1005290	2,510	738	49	15.1	-	-
			1,200	53	22.6		
			1,139	33	34.5		
			1,219	47	25.9		

Note. Location labels refer to Figure 2a.

^aAffected by later deposition of ignimbrite. ^bHeight affected by uncertainties over pre-eruptive topography.

Basaltic cones and lava flow deposits have been erupted along faults to the south-east of the caldera and are themselves cut by later activity along the same faults (Figures 5a and 5b). Cones and lavas are closely attributed with each other, suggesting single events for emplacement of both cone and lava flows as is observed elsewhere in the rift (e.g., west of Fentale, east of Tulu Moje).

A feature inside the NE caldera wall is identified as the scoria cone associated with an ash-rich deposit (Figure 5a). This cone is cut by later activity on a fault and is located at the intersection between a fault and a sharp change in strike of the caldera wall.

3.3. Corbetti

The high-resolution DEM produced in this study (Figure 6) allows the identification of 30 craters across the Corbetti Volcanic Complex, an additional 14 to those mapped previously (Figure 6a; Lloyd, Biggs, Wilks, et al., 2018). Craters are distributed WNW-ESE across the complex in two broad swaths. The craters range in diameter from 150 to >1,500 m and are commonly highly elliptical, with long axes trending WNW-ESE and N-S. In several cases, multiple small craters are coalesced forming a longer depression (Figure 7a).

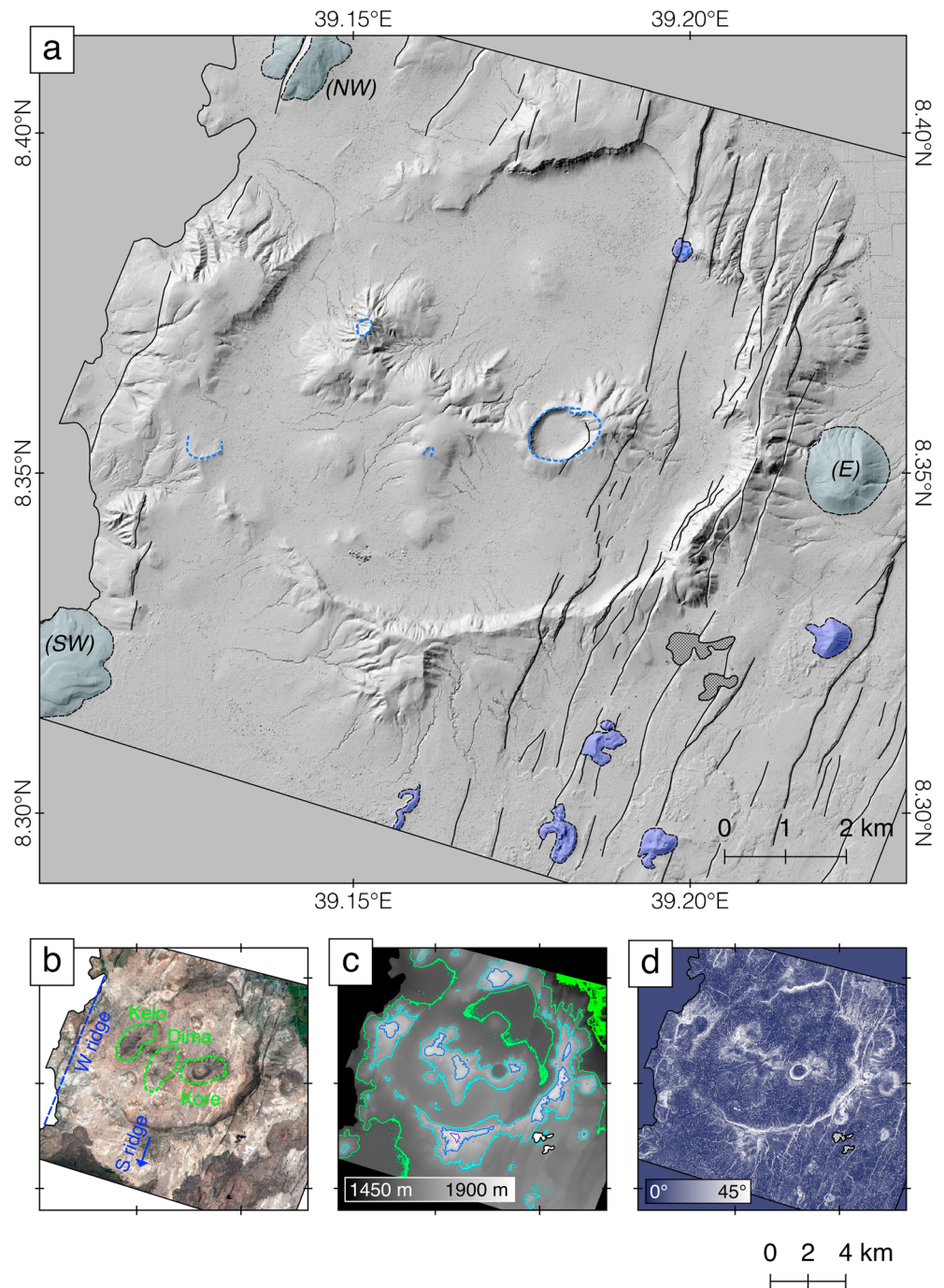


Figure 5. Maps derived from the digital elevation model of Gedemsa, clouds are masked in gray. (a) Hillshade map, illuminated from 300°N. Key features discussed in the text are highlighted, including basaltic scoria cones (blue), other notable deposits (gray), craters (blue dashed line), and faults (black line). (b) Pansharpened multispectral image of Gedemsa, with key ridges and domes labeled. (c) Elevation map, with contours every 100 m. (d) Slope map.

Urji (2,230 m) forms a lower and broader edifice than Chabbi (2,300 m) as shown on the elevation and slope DEMs (Figures 6c and 6d). This is in part due to Urji's predominately explosive history, creating an edifice mainly of ash, pumice, and other fall deposits. On the other hand, Chabbi's numerous effusive eruptions have created a steeper edifice mainly comprising obsidian lava coulees. Despite the greater flux from Chabbi over the last 2,300 years, the edifices of Urji (6.4 km³) and Chabbi (7.5 km³) are similar in volume (Table 3).

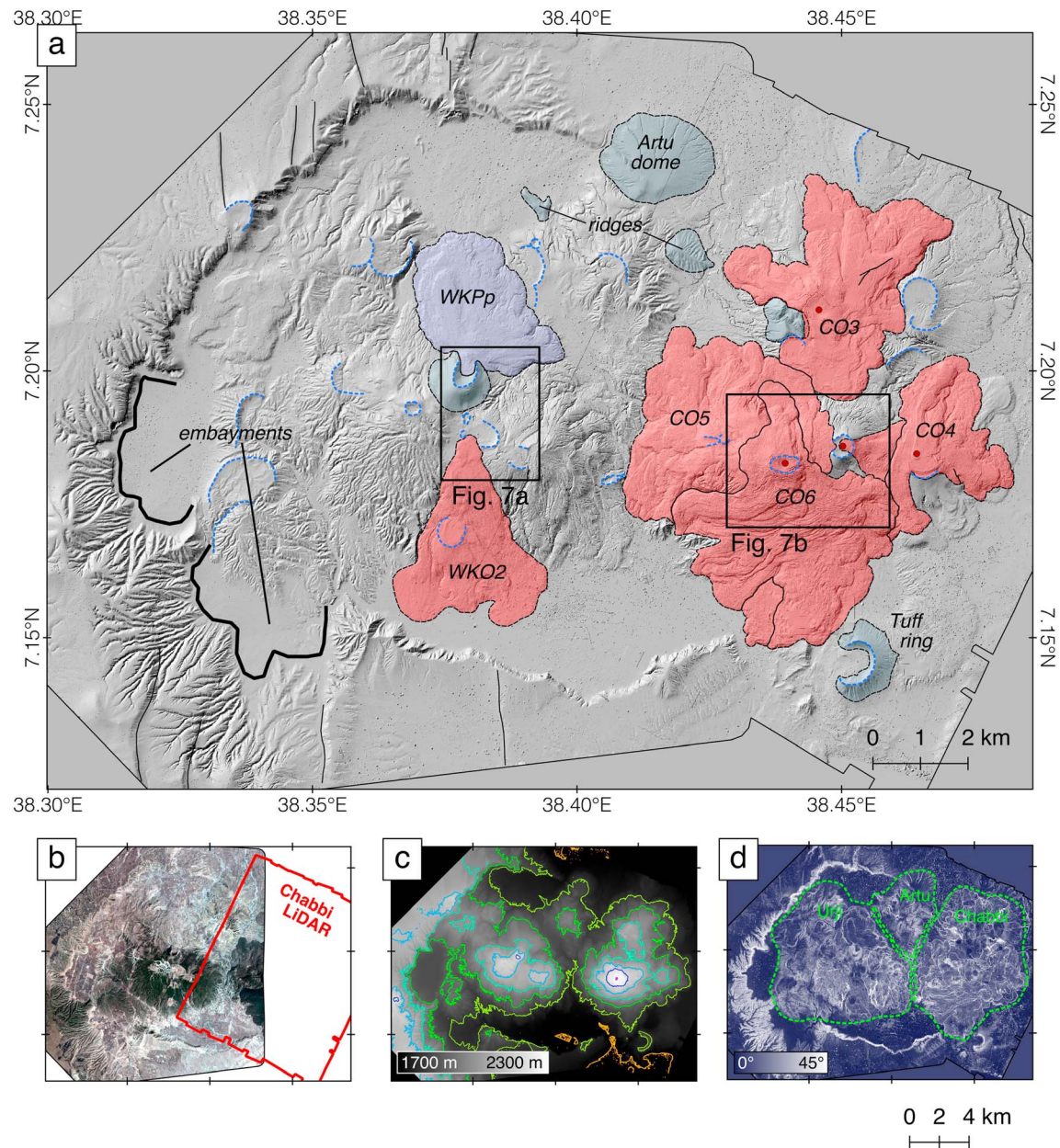


Figure 6. Maps derived from the digital elevation model of Corbetti. (a) Hillshade map, illuminated from 300°N. Key features discussed in the text are highlighted, including post-caldera coulees (red), pumice flow deposit (purple), other notable deposits (gray), craters (blue dashed line), faults (black line), and coulee vents (red circles). The speckled effect is produced by vegetation which is largely below the resolution of the digital elevation model. (b) Pansharpened multispectral image of Urji and the limits of the Chabbi lidar data set. (c) Elevation map, with contours every 100 m. (d) Slope map, with Artu, Urji, and Chabbi edifices labeled.

The highly incised surface morphology of Urji suggests an older age than Chabbi on average, as well as the softer material with which it is formed (Figure 6a). Two main domes form the bulk of Urji's edifice (Figures 6c and 6d), aligned along with the southern swath of craters WNW-ENE. A large cone creates the highest point on the edifice, mapped by Rapprich et al. (2016) as the Wendo Koshe young cone. Two flow deposits are apparent on Urji. A high-relief, lobate deposit originates from northern rim of the summit cone and crater, mapped by Rapprich et al. (2016) as a pumice deposit associated with the Wendo Koshe Younger Pumice (WKYP) emplaced predominantly by flow (WKPP, Figure 6a). To the south of the summit cone and emanating from between the two main domes, a lower relief obsidian coulee covers the flank of Urji, including a crater part way down the slope (WKO2, Figure 6a).

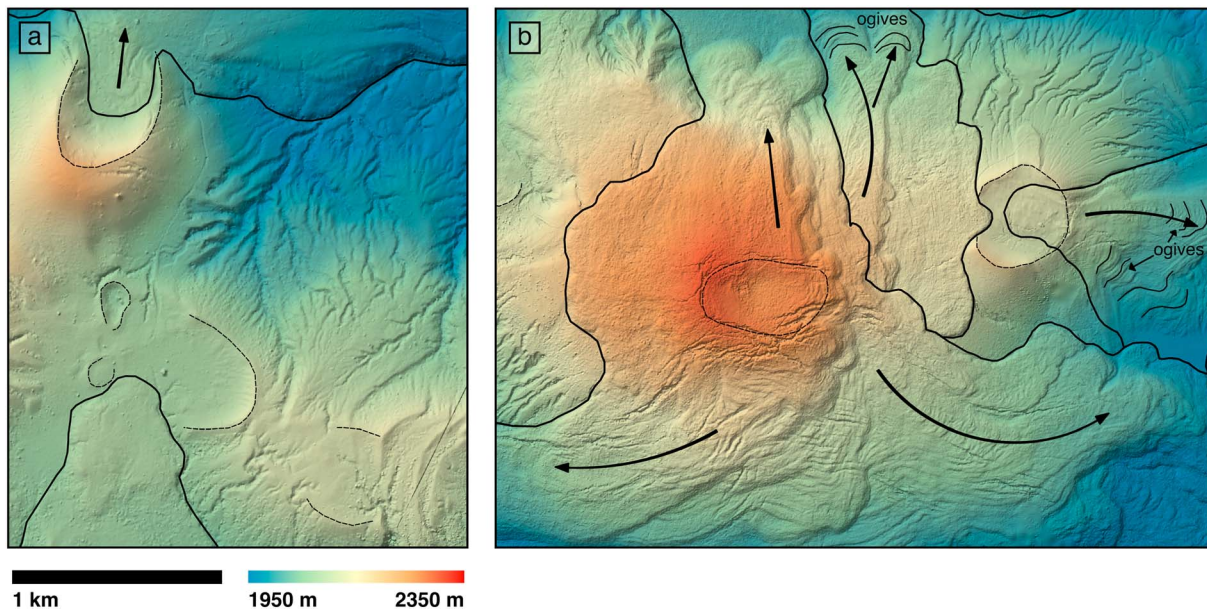


Figure 7. Combined hillshade and elevation map of craters (dotted lines) and flow deposits (solid lines) mapped in this study from (a) Urji and (b) Chabbi.

The large obsidian coulees on Chabbi are clearly recognizable on the hillshade DEM (Figure 6a) as are their ogives, which reveal the direction of flow in some places (Figure 7b). The coulees have originated from single vents, many of which are large, elongated craters that may be the product of preceding explosive activity. The source regions of other coulees have been fully buried, however the topography is depressed possibly indicating the presence of a crater (Figure 7b). Coulees partially cover preexisting, incised deposits which form steep cones at the sides of the coulee edge, for example, on the NW and SW flanks of Chabbi.

The obsidian coulees form large lobes in multiple directions as they radiate out from the source, with typical widths of 300–500 m. Typical runout distances are 2–3 km. The most recent obsidian coulee (CO6) is of similar magnitude (0.47 km^3 ; Table 3) to the Dense Rock Equivalent of WKYP (0.4 km^3 ; Rappich et al., 2016). There are six mapped lava coulees associated with Chabbi—assuming a similar magnitude for each coulee, $\sim 2.4 \text{ km}^3$ of lava is accounted for. The total volume of the Chabbi edifice is 7.5 km^3 , implying a number of completely buried coulees and/or extensive explosive deposits to account for the remaining erupted volume.

The older edifice of Artu is smaller (0.6 km^3) but hosts several large craters and two ridges running \sim WNW-ESE (Figure 6a). A broad dome (diameter $\sim 2 \text{ km}$, height $\sim 100 \text{ m}$) to the north is located along the extension of the northern rim of the caldera. Much of the original Artu edifice may now be buried by sediment filling the caldera.

The Corbetti caldera is irregular and segmented, delineated by a steep cliff along its northern and southern rim and a broad, incised slope on the western side (Figures 6a and 6d). The overall shape is governed by linear features, including a NE-SW trending wall on the western side and a WNW-ESE trending walls on the north and south. As noted by previous authors, the eastern side of the caldera is covered by the Chabbi edifice (e.g., Di Paola, 1971); the presence or absence of an original caldera rim on this side cannot be confirmed.

The elevation of the caldera floor ranges from 1,700 to 1,850 m, lowest in the area south of Urji and Chabbi and highest to the west of Urji (Figure 6c). The area outside of the caldera on the west is also elevated with respect to the area to the south of the caldera. Activity of rift-related faults may have caused the central section of the complex to subside with respect to the areas to the west. Later deposition may also have been greater in the western side of the caldera.

The western side of the complex is cut by numerous normal faults visible to the north and south of the volcano but no offsets visible within the caldera. Faults have not disrupted volcanic products and sedimentary deposits, implying either recent deposition, a lack of recent fault activity, or the discontinuation of faults at

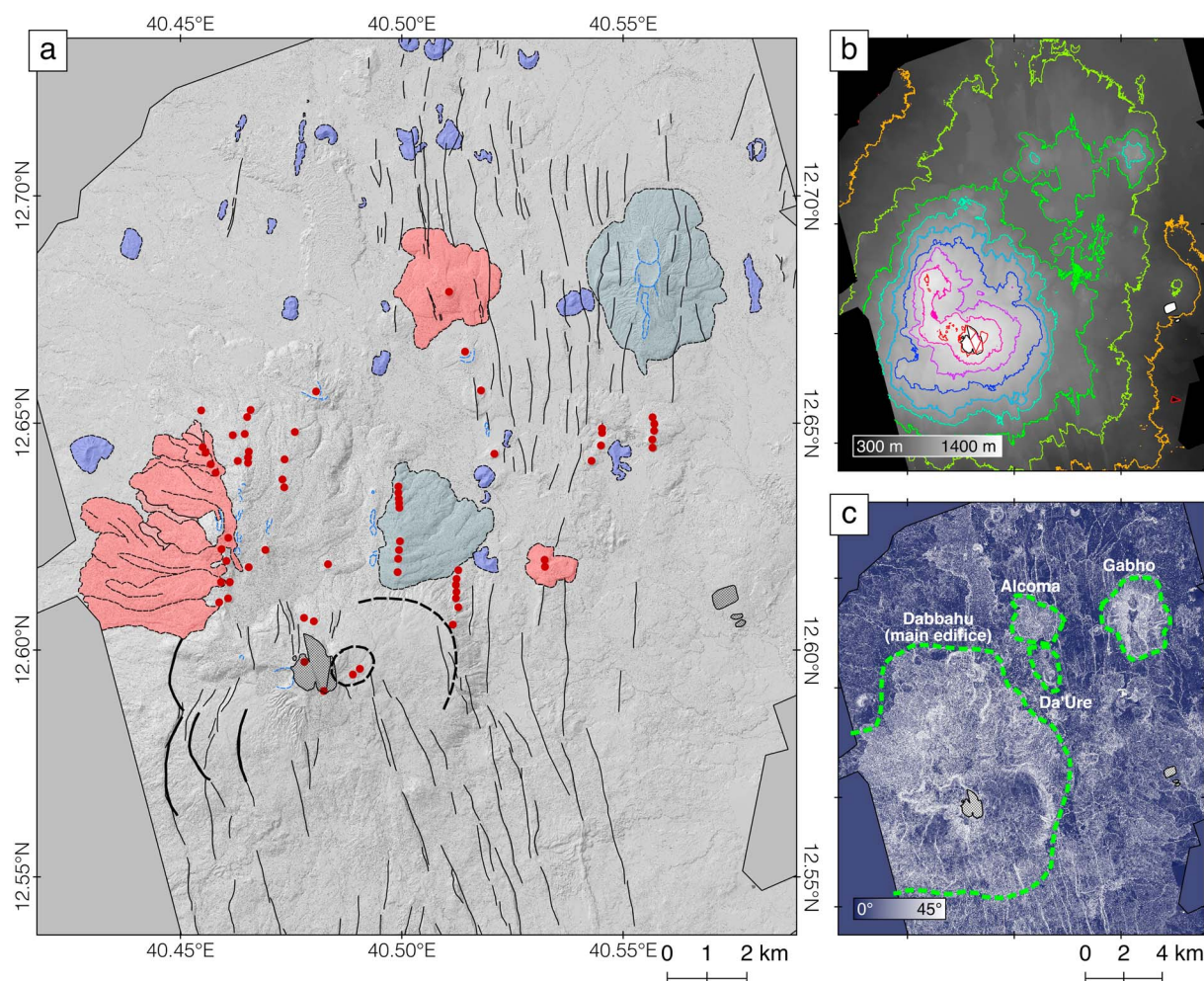


Figure 8. Maps derived from the lidar digital elevation model of Dabbahu, data gaps are masked in gray. (a) Hillshade map, illuminated from 300°N. Key features discussed in the text are highlighted, including post-caldera coulees (red), basaltic scoria cones (blue), other flow deposits (gray), craters (blue dashed line), faults (thin black line), possible caldera faults (thick black line), proposed caldera limits (dashed black line), and silicic vents (red circles). (b) Elevation map, with contours every 100 m. (c) Slope map, with the central Dabbahu edifice and Alcoma, Da'Ure, and Gab'ho satellite centers labeled.

the volcanic margins. There is a notable embayment in the south-western corner of the caldera, forming a highly eroded, broad slope adjacent to a steep cliff (Figure 6a).

The intersection of normal faults with the caldera rim is coincident with areas of caldera rim deflection. This is most clearly seen in the NW and SW of the caldera, where small offsets in the caldera rim are aligned with regional faults and the northern corner of the caldera is coincident with intersection of a fault (Figure 6a).

Basaltic volcanism is less prevalent in the Corbetti area than around Fentale or Gedemsa—no basaltic volcanism has been identified within the caldera limits. Scoria cones can be found to the south east near the town of Awassa, and to the north toward O'a caldera along regional faults (see Figure 9).

3.4. Dabbahu

The edifice of Dabbahu is tall and steep (Table 2), with two main summits aligned NW-SE (1,320 and 1,370 m; Figure 8). The summits are linked by ridges trending E-W and N-S, with a lower, parallel N-S ridge to the east. The northern flank of the edifice is much steeper on average than the south (Figure 8c). An area to the east of the highest summit has a relatively shallow slope surrounded by a steep cliff (Figures 8b and 8c)—this is an area of proposed caldera in-fill (Field et al., 2013). A number of satellite centers are located to the northeast of the main edifice, each of which is elongated in the N-S direction.

Table 5

Apparent Yield Strengths, From Measurements of Thickness and Slope Using Equation (1) (Assuming a Bulk Density of 2,300 kg/m³), of Three Lava Coulees From Fentale Identified in the Field

Location	UTM of vent(s) (easting, northing)	Thickness, m	Slope, deg	Apparent yield strength, kPa
Western ridge	4440089, 1005138 4440338, 1005122?	15–40	26	150–400
North west	4441137, 1006918?	15–40	5–7	30–110
SE dome	4444570, 1003332 4445276, 1002800	5–10	12	23–47

Note. Thickness was estimated from the difference in elevation between the coulee and an estimated pre-eruptive surface.

The DEM shows curved faults in the southwest of the study area that form rims of proposed caldera structures. Offsets of ~10 m cut through the ~E-W ridge protruding from the main summit, suggesting movement on the curved fault more recently than formation of the ridge. In the case that the curved faults in the southwest form an elliptical caldera with the buried caldera rim to the northeast (dashed line, Figure 8a), the proposed caldera would have a long-axis width of 6–8 km. This caldera would be comparable in size to many of those in the MER. The ellipticity of this caldera would trend at 45/225–60/240°, oblique to local fault trends.

Many of the vents, craters, and scoria cones are closely associated in N-S fissure swarms. Craters and coulee vents are colocated, for example, on the western N-S ridge (Figure 8a), suggesting a combination of explosive and effusive eruptions within the same event. Separate coulees are difficult to identify along the ridge, although a difference in color observed from freely available satellite imagery (via Google Earth) is able to distinguish between a set of recent coulees and the preexisting ridge. The ridge therefore composes of more than one episode of activity from N-S trending fissures. The coulees form narrow (300–500 m) channels with runouts of ~3.5 km and host ogives and lobes similar to those on Fentale and Corbetti. The satellite center of Alcoma also hosts a broad coulee, which radiates in many directions, forming several lobes (Figure 8a).

A line of craters aligned N-S are parallel to more rhyolite vents forming a N-S ridge in the north east of the main edifice and feeding a series of flow deposits (Figure 8a). Another line of nested craters runs through the center of the Gab'ho edifice to the north east, which is also cut by numerous faults (Figure 8a).

The majority of identifiable silicic vents and craters are to the north of the main summit of Dabbahu. Older deposits of trachyte/trachyandesites, and rhyolites to the southwest (Field et al., 2013) may suggest a progression of silicic activity from the southwest to the northeast over time. This remains a hypothesis to test by field work, dating, and further mapping.

Extensive basaltic trachyandesites are found across the area in the form of scoria cones and associated lavas. The cones are commonly aligned along faults and/or in N-S fissures (Figure 8a). The cones are larger than the basaltic scoria cones observed near Gedemsa. While scoria cones are not identified on the silicic edifices, Field et al. (2013) mapped deposits of basaltic trachandesite across a large area on the eastern flank of the main edifice and suggested that the bulk of the main edifice was basaltic on the basis of exposure in river beds.

Faults are concentrated to the south of the main Dabbahu edifice and to the northeast among the satellite centers. To the south they trend approximately NNW-SSE whereas to the northeast they trend ~N-S with some examples of NNE-SSW (Figure 8a). While faults cause large offsets on the southern flank of the edifice, they do not cut the more recent deposits on the northern flank. Concentration of faults in localized areas, each with a characteristic orientation, is common across the Afar region (see Figure 12).

3.5. Flow Morphometry

The lava coulees on Fentale and Corbetti display distinctive morphology which provides insight into the eruptive dynamics of each system. Table 5 shows the estimates for apparent yield strengths on the basis of deposit thickness and slope for three of the coulees on Fentale (using equation (1) from section 2). Yield strengths are not estimated for the larger coulees on Corbetti due to uncertainties over pre-eruptive surface and variable slope/thickness. The estimates from Fentale range from 20 to 390 kPa; the lower estimates are

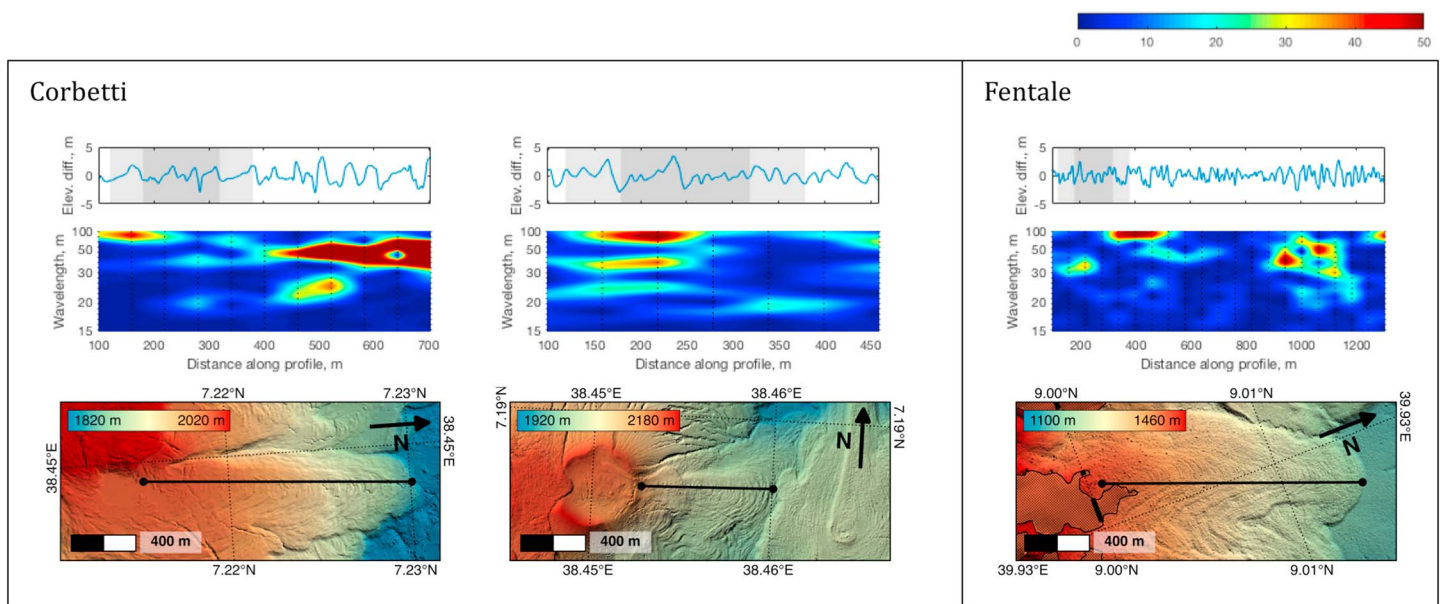


Figure 9. (top) Profiles along lava coulees from Corbetti and Fentale exhibiting wrinkles/ogives. (middle) Contoured periodograms showing the dominant wavelength of ogives with distance along profile, with two example windows for each profile shaded gray. (bottom) Combined hillshade and elevation maps of coulees showing ogives and profile lines.

in the approximate range for dacites (e.g., 30–70 kPa; Pyle & Elliott, 2006) and the upper estimates are in the range for rhyolites and trachytes (e.g., 80–400 kPa; Moore et al., 1978, Wadge & Lopes, 1991).

Figure 9 shows profiles along coulees hosting ogives and results of analysis for two coulees on Corbetti and one on Fentale. Contoured periodograms show the Fast Fourier Transform (see section 2) results by relative power (arbitrary scale) of fold wavelengths at each window location along the length of the flows. Ogives of wavelength 20–100 m are observed. Multiple generations of folds are visible for each coulee. The Corbetti coulees exhibit folds at the scale of 80–100, 30–50, and 22–28 m, with a faint signal from small-scale folds of wavelength ~17–20 m. The folds in the first panel progress to longer wavelengths down-slope. In contrast, the longer wavelengths are more dominant up-slope in the second panel, where the shorter wavelength folds are clearer down slope. This may indicate differences in flow thickness along the flow, and therefore thickness of the cooling surface.

The wavelengths of folds on the Fentale lava coulee are less consistent, however there exist folds of similar wavelengths to those observed on Corbetti. Folds of wavelength 30–50 and 80–100 m are observed early in the profile and reappear toward the end of the coulee, along with shorter wavelengths of 18–25 m.

The abundant levees at Fentale enable further constraints on lava rheology. The widths of leveed channels on Fentale are plotted against the average slope of the channel in Figure 10. The average slope of the channel is a proxy for the slope of the pre-eruptive surface, assuming an approximately constant thickness. Narrow channels form on steeper slopes, while broader channels form on shallow slopes.

The predicted relationship between channel width and angle of slope from the Kerr et al. (2006) model is shown in Figure 10 for a range of Φ values (see equations (2)–(4) in section 2). The data are consistent with the general shape of the relationship, for Φ values of ~20–100 m. The panel in Figure 10 presents Φ values for a range of viscosities and flow rates, assuming a density difference of $2,300 \text{ kg/m}^3$, an effective yield strength of the cooled crust of $3 \times 10^5 \text{ Pa}$ (Castruccio et al., 2013; Fink & Griffiths, 1998) and a thermal diffusivity of $5.5 \times 10^{-7} \text{ m}^2/\text{s}$ (Romine et al., 2012). For maximum Φ values of 100 m, the maximum viscosity is $\sim 10^{11} \text{ Pa s}$ for a flow rate of $0.02 \text{ m}^3/\text{s}$ and $\sim 10^8 \text{ Pa s}$ for a flow rate of $2 \text{ m}^3/\text{s}$.

4. Discussion

Having assessed volcanic features and observed previously unidentified deposits, we use the DEMs to compare centers along the length of the MER, and between the MER volcanoes and Dabbahu. We compare

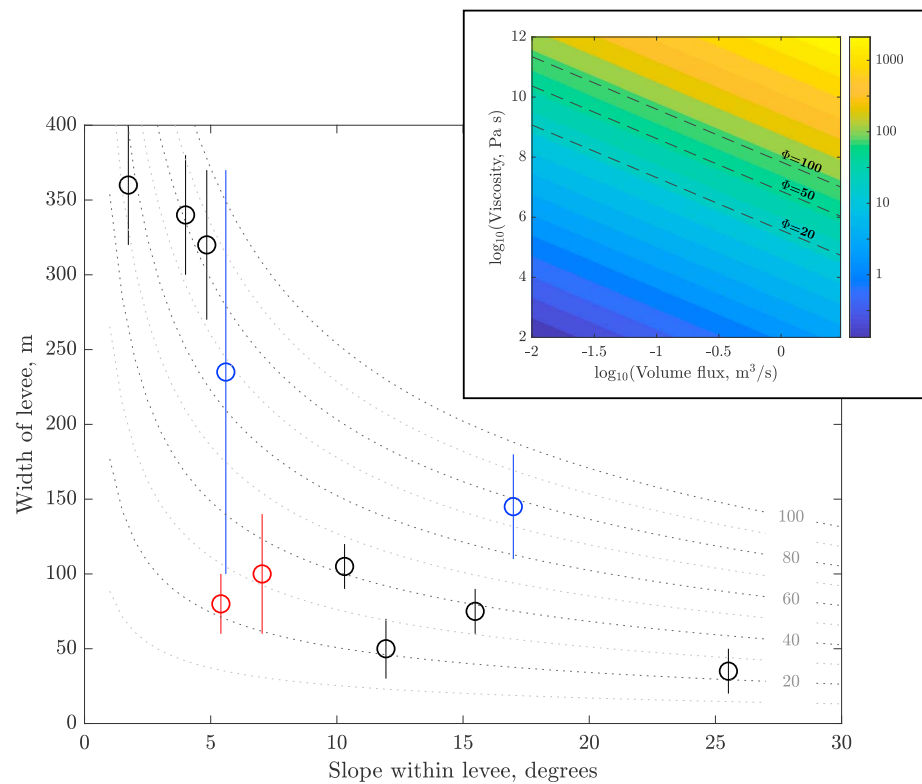


Figure 10. Relationship between levee width and slope within levees for 11 sets of levees on Fentale, including pre- and post-caldera coulees. In two coulees, two sets of levees are found at different distances from the vent—these are identified in red and blue. Dotted lines show the relationship predicted by equations (2)–(4) for $\Phi = 10$ –100 defined in equation (4) (section 3), a coefficient combining material properties of the lava and the volume flux of the eruption. (panel) Dependency of Φ on volume flux and viscosity according to equation (4), assuming values of density ($2,300 \text{ kg/m}^3$), yield strength ($3 \times 10^5 \text{ Pa}$) and thermal diffusivity ($5.5 \times 10^{-7} \text{ m}^2/\text{s}$).

caldera architecture (section 4.1), identify vent and crater alignments (section 4.2), estimate eruptive volumes and frequencies along the rift (section 4.3), and assess the morphometry of peralkaline lava deposits (section 4.4).

Figure 11 shows structural observations of the three MER volcanoes in this study, alongside two volcanoes previously studied using remote sensing. Aluto volcano has been the subject of a number of recent studies (e.g., Gleeson et al., 2017; Hutchison, Biggs, et al., 2016; Hutchison, Pyle, et al., 2016; Samrock et al., 2015; Wilks et al., 2017), including the use of a lidar DEM to identify structural features (Hutchison et al., 2015). The geological evolution of Boset volcano has been studied by Sieburg et al. (2017) using a lidar DEM in addition to field work, geochemistry and geochronology. Figure 12 shows structural observations of Dabbahu within the context of the Afar region, with faults across the region redrawn using the Aster Global DEM and previously published maps (Barberi & Varet, 1977; Donovan et al., 2018).

4.1. Caldera Architecture

The overall structures of Gedemsa, Corbetti, and Fentale vary widely. The edifice of Fentale is taller than that of Gedemsa and Corbetti, and while Fentale's footprint is similar to that of Gedemsa, the footprint of Corbetti is notably larger (Table 2). The difference in edifice structure is largely due to the difference in caldera architecture—the caldera of Fentale is deep and narrow, whereas the formation of the broad calderas of Corbetti and Gedemsa were presumably accompanied by the subsidence of a larger proportion of their ancestral edifices. The regular and elliptical shape of Fentale's caldera is also in contrast to the calderas of Gedemsa and Corbetti, which are heavily and variably eroded, and partially covered by later deposition of lake sediments. This may be related to the influence of faults, erosion rates, and age of the calderas.

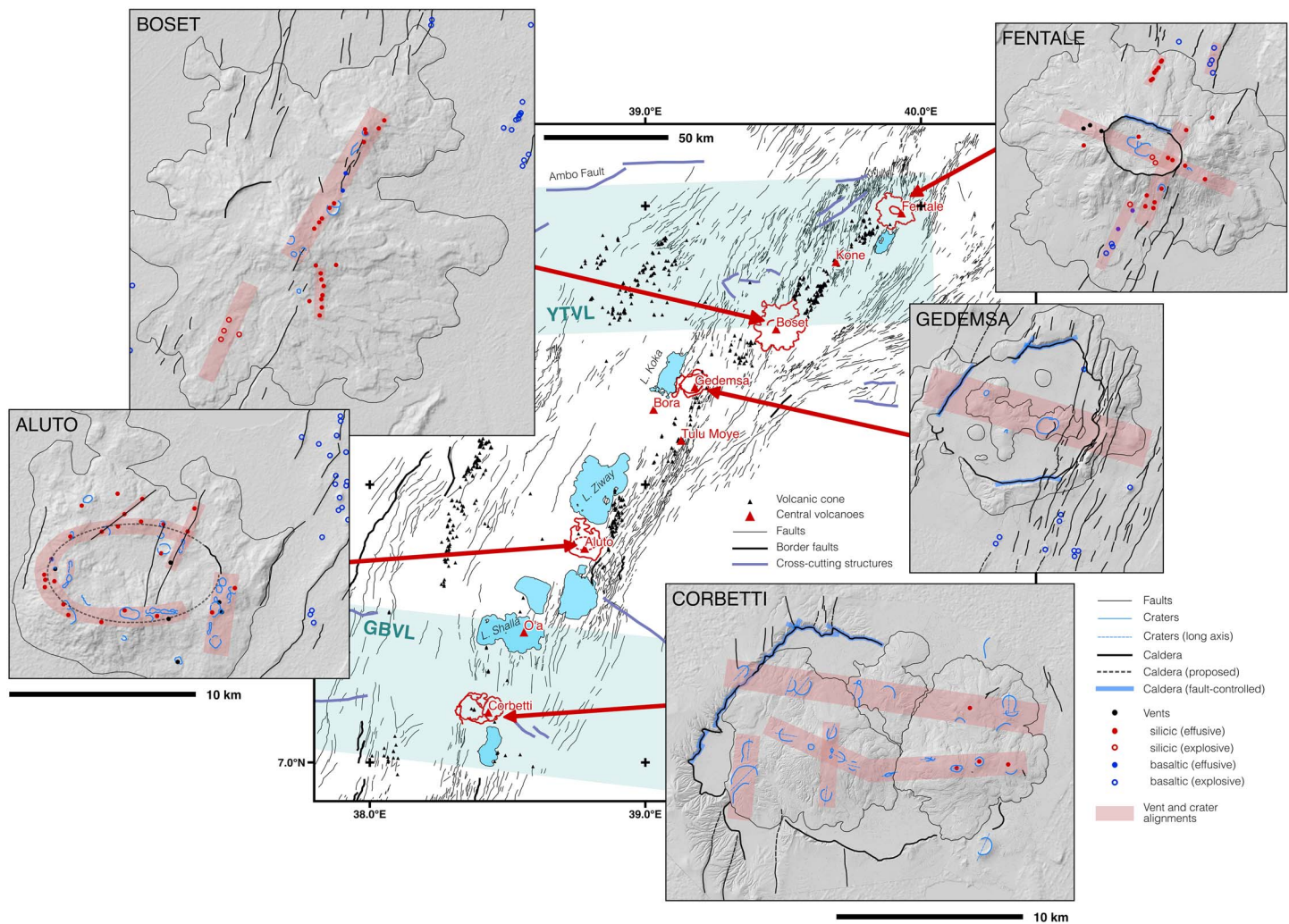


Figure 11. Map of the Main Ethiopian Rift, including volcanoes, faults, and border faults (Agostini et al., 2011; updated version available from <http://ethiopianrift.igg.cnr.it/>). Panels display structural associations, vents, and craters for the volcanoes in this study (right) and two other volcanoes for comparison (right). Hillshade products from the Aster Global Digital Elevation Model (product of METI and NASA) are used to display the topography of Boset and Aluto. GBVL = Goba-Bonga volcano-tectonic lineament; YTVL = Yerer-Tulu Wellel volcano-tectonic lineament.

Only short segments of the calderas at Aluto and Boset are unburied. Hutchison et al. (2015) proposed the approximate location of a caldera fault at Aluto on the basis of vent and crater locations. The proposed caldera is larger than that of Fentale and the low and broad edifice of Aluto may suggest a broad and shallow underlying caldera similar to those of Gedemsa and Corbetti.

Several arced structures on Dabbahu suggest the presence of multiple calderas in addition to summit pit craters. Field et al. (2013) proposed three overlapping calderas, similar to the nested calderas mapped at Kone Volcanic Complex in the MER (Rampey et al., 2010). The size of the nested calderas at Dabbahu (~3–8 km wide) is similar to those in the MER. Subsequent burial of the structures by post-caldera activity has produced an overall structure analogous to Boset, with fissure eruptions of both silicic and basaltic material.

Gedemsa and Corbetti host several embayments and offsets leading to highly irregular shapes. These embayments and offsets are partly influenced by rift-related normal faults which cut the calderas to differing degrees (Figure 11). The normal faults form limits to the depression, causing the caldera rim to be locally deflected. The faults impinge on the caldera rim at points of greatest curvature, indicating a possible control on the extent of subsidence.

In addition to faults offsetting caldera rims at various points, all three MER volcanoes from this study display linear sections of caldera rim controlled by underlying structures (highlighted in blue, Figure 11). At Fentale

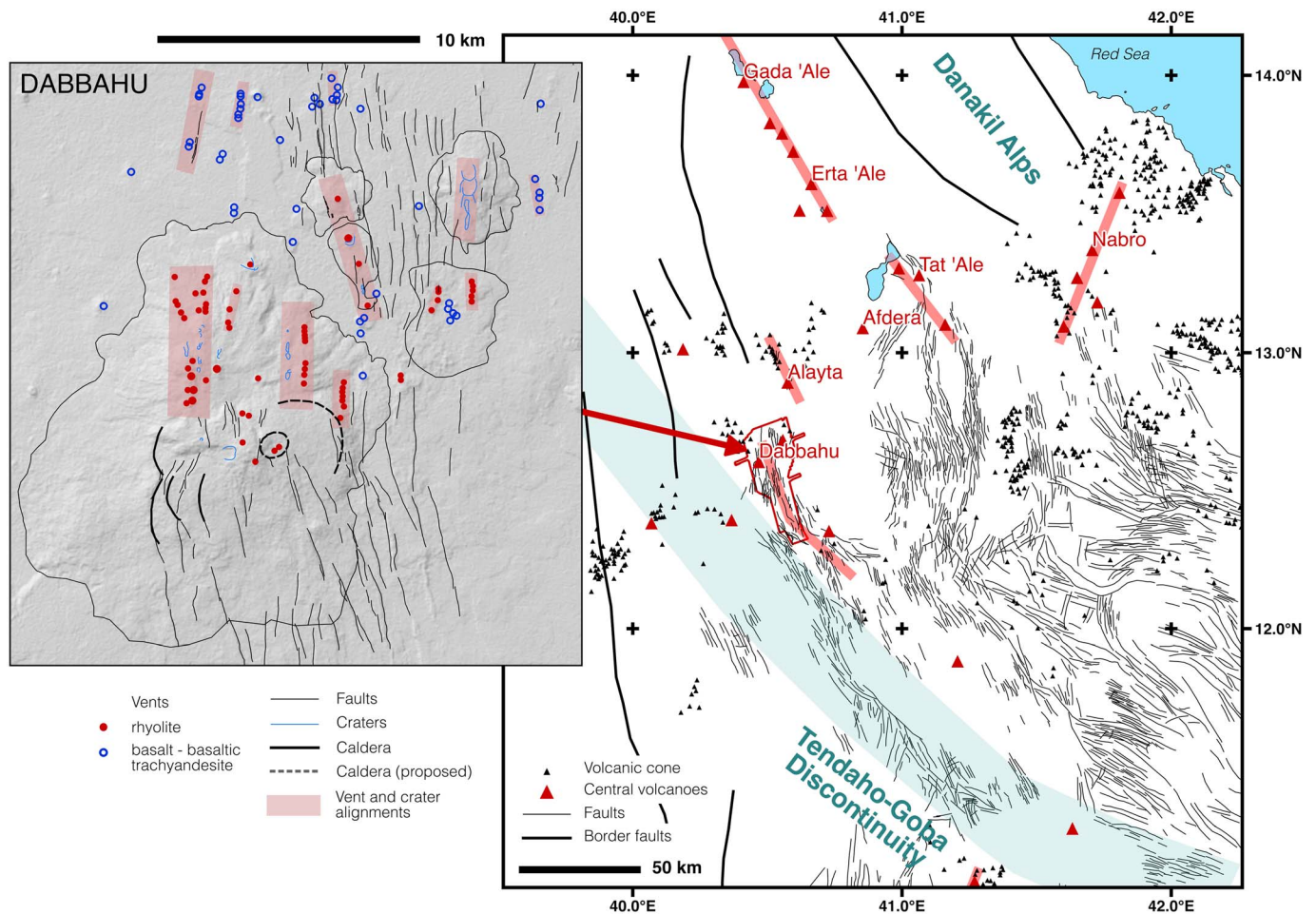


Figure 12. Map of the Afar, including volcanoes and faults (redrawn from Barberi & Varet, 1977; Donovan et al., 2018, using the Aster Global Digital Elevation Model product from METI and NASA). (panel) Dabbahu volcano, displaying structural associations, vents, and craters on a hillshade map derived from the Aster Global Digital Elevation Model.

and Corbetti, these proposed fault-controlled sections are parallel to other structural alignments. In controlling the large-scale shape of the caldera, these fault-controlled sections affect the long-axis orientation of the calderas.

Figure 13 displays rose diagrams which show the changing strike of regional faults as well as the long-axis direction for each caldera. The orientation of the main proposed caldera for Dabbahu is also indicated. In every case except for Fentale, the caldera long-axis is cross-cutting but not orthogonal to the local normal faults. At Fentale, the long-axis is orthogonal to the faults but parallel to an alignment of vents and the linear northern rim of the caldera.

Ellipticity of calderas is influenced by the local stress regime, preexisting structures, multiple collapses, and post-caldera processes (Holohan et al., 2005; Robertson et al., 2015). Caldera ellipticity in the MER was related to natural extension-related strain by Casey et al. (2006). Examples of faults controlling the geometry of calderas are found in Indonesia (Ranau and Toba; Bellier & Sébrier, 1994), New Zealand (Spinks et al., 2005), and Kenya (Robertson et al., 2015).

The phenomenon was reproduced in analog experiments by Holohan et al. (2005) in which a number of key observations were made. Preexisting faults commonly became caldera-bounding faults, truncating or distorting the otherwise preferred elliptical structure of the caldera. The nearest regional faults accommodated some of the subsidence from caldera collapse, and faults pervading the caldera center caused piecemeal collapse as subsidence was accommodated variably between fault blocks. Our observations are consistent with similar impacts of pervasive faulting on the formation of calderas in the MER, with rift-related normal

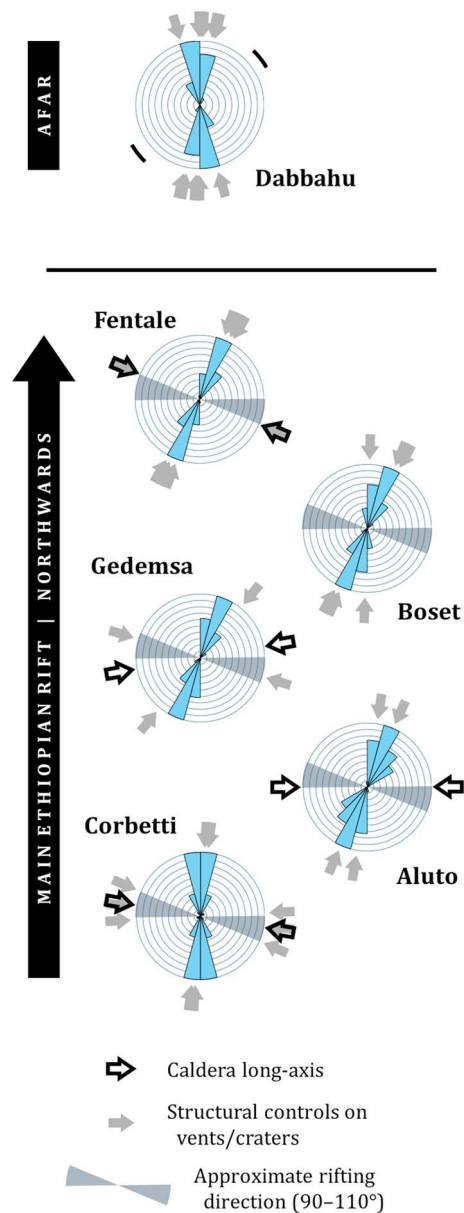


Figure 13. Rose diagrams of fault orientations (blue) around each volcanic center, orientations of structural alignments and caldera long-axis shown by arrows. The long-axis of the postulated caldera at Dabbahu is shown by a black line. Approximate spreading direction in the Main Ethiopian Rift is shown in gray (Saria et al., 2014).

faults truncating and distorting caldera geometry and cross-cutting structures becoming caldera-bounding faults.

For cross-cutting structures to influence the formation of calderas and location of eruptions, they must be long-term structures and have shallow manifestations. A number of known cross-cutting structures exist around the MER (Figure 11), including the Yerer-Tulu Wellet volcano-tectonic lineament (T. Abebe et al., 1995, 1998) and the Goba-Bonga volcano-tectonic lineament (Abbate & Sagri, 1980; Corti, Sani, et al., 2018). Acocella et al. (2002) mapped many left-lateral, E-W trending structures on the rift flanks and associated them with the ellipticity of calderas within the rift. These structures may have been reactivated during rifting, and could have formed pull-apart structures encouraging the formation of elliptical magma reservoirs in specific locations (Acocella et al., 2002).

Along-axis variations in rifting stage may affect caldera architecture and the extent to which cross-cutting structures influence their formation. The influence of such preexisting structures is likely larger in early stages of rifting than late stages (e.g., Corti, Molin, et al., 2018). This is arguably supported by the simpler geometry of Fentale's caldera in the northern MER (late stage rifting) compared to the geometry of Corbetti in the southern MER (earlier stage). The mode of caldera formation may also be influenced by rifting stage, with simple piston collapse forming Fentale's regular caldera and possibly Dabbahu's pit craters, compared to complex piecemeal collapse of Gedemsa and Corbetti's larger, irregular calderas.

Variable erosion of the caldera rims and large irregularities in caldera shape may suggest the presence of more than one collapse event. This hypothesis is supported at Gedemsa by the existence of multiple ignimbrites and extensive pumice deposits (Fontijn et al., 2018; Thrall, 1973). The abundance of incision along the western rim of the Corbetti caldera compared to the north and south may be due to hydrology or local geology (i.e., weaker substrate), or possibly an older age. In this case, multiple collapse events may be responsible.

Slope failure during the post-caldera phases of each volcano could also account for the observations of the influence of faults and irregularities in shape—in this case, caldera geometry is modified by erosion with slope failure likely to be bounded by faults as planes of weakness. Given the age of the MER calderas (~170–320 ka; Hutchison, Fusillo, et al., 2016), post-caldera modification is likely an important factor in caldera morphology. Further work is required to constrain the number of collapse events, the relative importance of faults in controlling subsidence, and the extent of post-caldera modification at each volcano.

4.2. Locations of Eruptions

The volcanoes each show structural controls on the locations of eruption, as identified by vents, domes, and craters. Post-caldera activity at Fentale, Gedemsa, and Corbetti is frequently aligned along cross-rift structures (Figure 11). At Fentale, several craters and silicic vents, post- and pre-caldera, align parallel to the caldera long-axis (WNW-ESE) and in line with an observed steam vent. At Gedemsa, post-caldera domes delineate a WNW-ESE alignment, and at Corbetti there exist two or three swaths of craters aligned from WNW-ESE to ~E-W (Figure 11).

Contrastingly, vents and craters on Aluto follow a proposed caldera rim, which is now buried under subsequent deposition from eruptions (Hutchison et al., 2015; Figure 11). Caldera-aligned activity is not observed at other volcanoes, except for the basaltic scoria cone along the north-east rim of Gedemsa (Figures 5a and

11). The majority of vents and craters on Boset are aligned along the same axis, running parallel to rift-related faults. Vents are not identified along the buried caldera rim, nor are they found aligned with cross-rift structures. Studies of seismic anisotropy at Corbetti and Aluto show fast shear-wave polarizations parallel to cross-cutting structures—in the case of Corbetti, parallel to the Wendo Genet fault scarp (~NW-SE; Lloyd, Biggs, Wilks, et al., 2018), and in the case of Aluto, parallel to NE-SW alignments of vents (Figure 11; Nowacki et al., 2018).

Rift-parallel trends in activity are observed at each volcano, commonly in line with regional faults to the north and/or south of the edifice. A number of silicic vents at Fentale are aligned NNE-SSW along a rift-parallel trend on the eastern side of the edifice (Figures 2a and 11), along with a newly reported cluster of domes aligned in the same direction (Figure 2c). Basaltic vents to the south of the edifice are also aligned parallel to the rift, along with a pumice deposit.

At Gedemsa, the westernmost intra-caldera dome (Kelo) strikes NE-SW in line with a regional fault which offsets the caldera rim (Figure 9). At Corbetti, a number of craters have a long-axis trending N-S and are aligned in the same direction, parallel to local, rift-related faults. These are common on the western side of the edifice, where the regional faults are most abundant (Figure 11). The vents of Dabbahu are dominantly aligned parallel to local faults, similar to Boset (Figure 12).

The rose diagrams in Figure 13 compile these observations and compare orientations of the rift-related faults, caldera long axes, structural alignments of vents and craters, and the spreading direction in the MER (Saria et al., 2014). Fault orientation is N-S at Corbetti but consistently NNE-SSW to the north. Most structural alignments are parallel to the rift-related faults. Cross-cutting structural controls, where they exist, are mainly parallel to the long-axis of each caldera except at Gedemsa, which combines several structural orientations.

While caldera ellipticity may suggest an important role for cross-cutting structures in forming elliptical magma reservoirs, the absence of cross-cutting alignments at Boset suggests that they are not solely responsible for the location of major volcanoes along the rift. In addition, there are many cross-cutting structures observed on the rift flanks that apparently do not enable the formation of a magma reservoir along their strike.

Whether magma reservoirs are themselves influenced by cross-cutting structures or not, vent and crater locations are clearly influenced by these structures. Elsewhere in the rift, scoria cones and other erupted products are closely related to rift-related faults (e.g., Casey et al., 2006; Corti et al., 2013), as is the case at these volcanoes (Figures 11 and 13).

The propensity for vents and craters to follow faults and other structures in the MER indicates that structural control on eruption locations is greater than the influence of the local stress fields. The regional stress field encourages dike formation orthogonal to the rift-direction (Anderson, 1951; Guðmundsson, 1995; Nakamura, 1977). For most of the rift, this is difficult to distinguish from the trend of rift-related normal faults—vents and craters influenced by these faults are therefore also likely influenced by the regional stress field.

However, stress fields associated with edifice loading, pressurized magma reservoirs, and/or cylindrical conduits lead to radial dikes and therefore alignments of cones and craters (e.g., Muirhead et al., 2015; Wadge et al., 2016). The absence of these alignments, and the presence of cross-cutting alignments, suggests a strong structural control rather than influences of stress fields influenced by crustal loading or magma pressure, as found elsewhere in the rift (Wadge et al., 2016). Edifice loading is a significant feature for volcanoes with heights ~1–2 km (Wadge et al., 2016)—a combination of evacuation by caldera formation, ubiquitous normal faulting, and low eruptive rates lead to low heights of most MER volcanoes.

4.3. Volumes and Frequency of Eruptions

Figure 14 presents the number of vents and craters of various types for each MER center, estimates of the total volume erupted in the post-caldera phase, and published estimates for the ages of each caldera (Bigazzi et al., 1993; Hutchison, Fusillo, et al., 2016; Peccerillo et al., 2003; Sieburg et al., 2017; Williams et al., 2004). Caldera ages are associated with large uncertainties, particularly at Gedemsa, Boset, and Fentale—more dates are needed to constrain these ages further.

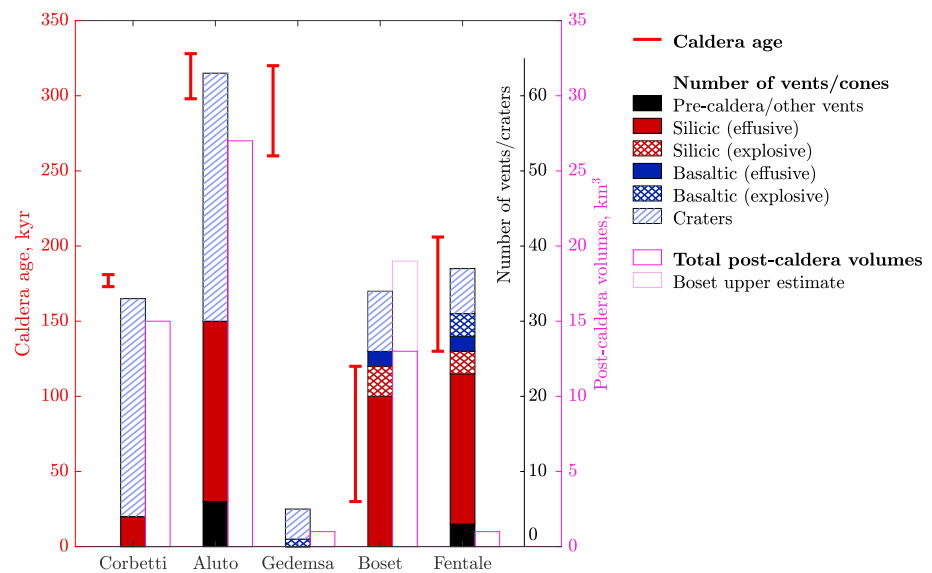


Figure 14. Bar graph displaying the number of vents, cones, and craters for each volcanic center alongside total post-caldera volumes and the age of each caldera.

Hutchison, Fusillo, et al. (2016) estimated the total post-caldera volume of Corbetti (15 km³), Aluto (27 km³), and Gedemsa (1 km³) using an SRTM 30 m-resolution DEM. These estimates agree with the volumes calculated in this study to the nearest 1 km³ (Table 3). Siegburg et al. (2017) published volumes for each eruptive phase at Boset. These volumes have been combined to give an estimate of the total volume for the post-caldera phase, allowing for uncertainty concerning the age of the caldera and therefore the identification of which phases post-date caldera formation.

The number of vents and craters observed at each center provides an insight into the frequency of eruptions at each volcano. Other factors affect the identification of vents and craters, including the burial of vents and craters by subsequent eruptions, and eruptions that retain no discernable vent or crater. Burial of vents and craters has occurred at Boset, Corbetti, and Dabbahu, a consequence of large eruptive volumes and high eruption frequencies. Gedemsa has produced post-caldera erupted deposits with very few observable vents and craters—this may be a consequence of post-emplacement erosion or immediate burial at time of emplacement.

Aluto hosts the most identifiable craters and vents of the five MER volcanoes in question. Corbetti, Fentale, and Boset host a similar number of craters and vents. Craters are common on Corbetti and Aluto, and less common on Boset and Fentale. Dabbahu hosts a large number of scoria cones and rhyolite vents, many of which feed coulees (Figure 12). The scoria cones at Dabbahu are basaltic trachyandesite in composition (Field et al., 2013)—more silicic than the basaltic scoria in the MER.

The closest basaltic cones or lava flow vents to Corbetti and Aluto are 2–3 km from the edifice, whereas basaltic eruptions have occurred on the edifice at both Boset and Fentale (Figure 11). At Boset, basaltic flows have been erupted from the central fissure between the two peaks, along which silicic flows have also been erupted. At Fentale, a basaltic eruption also led to the formation of fissures (Williams et al., 2004). The vents for this lava deposit are meters away from the newly observed pumice cone. Basaltic and silicic vents are also found close together at Dabbahu, where the main silicic vents are spread out between several satellite centers (Figure 12).

A scoria cone has been emplaced within the north east caldera rim at Gedemsa (Figures 5a and 11), and an historical basaltic eruption at Kone, in the north of the rift, occurred within the caldera. The lack of basaltic volcanism in the south at Corbetti and Aluto may suggest a shielding effect by the active peralkaline magma reservoirs (Fontijn et al., 2018; Jeffery et al., 2016; Mahood & Hildreth, 1986; Mahood, 1984), whereas the less active volcanoes to the north may have only small or temporarily active magma reservoirs.

The ages of the calderas at Fentale and Gedemsa are similar to those at Corbetti and Aluto, respectively, but the volcanoes have much lower post-caldera erupted volumes. This suggests a much lower eruptive flux on average over the past 300 kyr. Despite the age of Gedemsa's caldera, the volcano has deposited little in its post-caldera phase and features few vents/calderas, suggesting a paucity of activity. Fentale hosts a high number of vents and craters relative to its post-caldera erupted volume, suggesting high-frequency, low-volume eruptions.

Lava coulee volumes at Corbetti are as much as 10 times greater than those at Fentale (Table 3), a relationship which is reflected in the total post-caldera erupted volume (Figure 14). The six lava coulees observed on Chabbi account for less than half of the volume of the edifice, suggesting a number of vents and craters lay buried beneath subsequent deposits. The total post-caldera erupted volume is also likely to be much higher than indicated at Corbetti and Aluto, as explosive eruptions and large craters are common. Such eruptions deposit material over a wide area, and only thick, proximal deposits are accounted for using the DEMs.

The volume of the CO6 lava coulee on Chabbi (0.47 km^3) is similar to the volume of the pyroclastic deposit of the WKYP (0.4 km^3 dense rock equivalent; Rappich et al., 2016). WKYP was deposited at 2.3 ka and has been followed by four lava flows on Chabbi. An estimated combined volume from these eruptions is $\sim 2 \text{ km}^3$, giving an eruptive flux of $8.7 \times 10^5 \text{ m}^3/\text{year}$. The long-term volume flux is $8.3 \times 10^4 \text{ m}^3/\text{year}$ (15 km^3 over 180 kyr), an order of magnitude lower. This implies a greater flux in the volcano's recent history.

4.4. Morphology of Peralkaline Lava Flow Deposits

The impact of the proposed rheological difference of peralkaline magmas (due to the abundance of halogens and excess alkali resulting in depolymerization and lower viscosities compared to metaluminous silicic melts, e.g., Dingwell et al., 1998; Hess et al., 1995) on eruption dynamics and lava emplacement is poorly understood. The lava coulees on Fentale and Corbetti display distinctive morphology which provides insight into the eruptive dynamics of each system. Several large-volume coulees at Corbetti are erupted from single, large, elliptical craters, perhaps suggesting a prior explosive phase of eruption. The resulting flows spread in multiple directions and form large lobes. Craters and effusive vents are also collocated at Aluto and Dabbahu, (Figures 11 and 12), where lava flow deposits are smaller than at Corbetti. The Alcoma satellite center at Dabbahu is a larger coulee emplaced on a shallow slope, which forms large lobes similar to those at Corbetti (Figure 8).

Small-volume coulees are erupted at Fentale from multiple vents, the spacing of which varies from 200 to 2,000 m. Short spacing of vents is also observed on Boset (Figure 11) and Dabbahu (Figure 12). Post-caldera coulees commonly cease before reaching the flat plain surrounding Fentale's edifice. Considering both post- and pre-caldera coulees, downflow slope appears to be a dominant factor controlling flow width. Crossflow slope and confining topography are also expected to influence flow width (Peitersen & Crown, 1999; Rogers et al., 1996), however apart from isolated examples (e.g., narrow flow to the west of the SE dome) these factors are less important.

Ogives/folds form on the surface of a lava flow whose viscosity decreases with depth, as the product of compression within the solidifying crust of a flow as it progresses down slope (Fink, 1980; Fink & Fletcher, 1978). Ogives on coulees at Corbetti and Fentale have wavelengths of 20–100 m, similar to those previously noted on lava flow deposits of andesitic, dacitic, trachytic, and rhyolitic composition (e.g., Latutrie et al., 2017; Pyle & Elliott, 2006; Warner & Gregg, 2003). Shorter wavelength folds have been observed on dacite deposits (Lescinsky et al., 2007); post-emplacement erosion and weathering may have altered small-scale morphological features on the Corbetti and Fentale lava coulees.

Multiple generations of folds form as the solidifying crust thickens, lengthening the optimum wavelength for folds to form (Gregg et al., 1998). The ratio between successive generations of folds depends on the relative importance of crust thickening by cooling and by shortening, which itself depends on composition (Gregg et al., 1998). Crusts on rhyolite flows grow largely due to cooling; basaltic crusts grow largely due to shortening because of higher strain rates (Gregg et al., 1998). Ratios between successive fold wavelengths are therefore lower in rhyolites (1.4–2.2) compared to basalts (4.0–6.2). The folds on Corbetti and Fentale have ratios of 1.4–3.3, similar to those observed in rhyolite and dacite deposits elsewhere (Gregg et al., 1998; Pyle & Elliott, 2006).

Though the relationship between measured channel width and angle of slope at Fentale agrees with the Kerr et al. (2006) model, there is a range of possible Φ values (defined in equation (4), section 2; Figure 10). Values of Φ depend on material properties (density, yield strength, thermal diffusivity) as well as volumetric flow rate and viscosity. We have assumed that the rheology of every coulee forming a levee is similar. Narrow channels are more likely to be affected by confining topography, which presents an additional factor controlling the width of the flow—for this reason, narrower channels may be more narrow than expected from the theoretical relationship. In addition to a simple, planar pre-eruptive surface, the model assumes constant viscosity and flow rate and therefore does not account for pulses, blockages, and other complicating factors (e.g., Bailey et al., 2006). The model assumes that levees are formed due to yield stress, but other models of levee formation may apply, including the buildup of rubble (e.g., Bailey et al., 2006; Sparks et al., 1976). This may be particularly relevant for low yield stress lavas, including acrySTALLINE lavas similar to those found in the MER. Experimental studies on the rheology of peralkaline rhyolites, similar to those at Fentale (Gibson, 1974; Webster et al., 1993) and elsewhere in the rift (Gibson, 1972; F. Giordano et al., 2014; Peccerillo et al., 2007), suggest that their viscosities are relatively low— $\sim 10^{5.5}$ Pa s for a volatile-free peralkaline rhyolite magma at 1223 °C compared to $\sim 10^8$ Pa s for a calc-alkaline rhyolite (Di Genova et al., 2013; D. Giordano et al., 2008; Hughes et al., 2017). Viscosities of lava at time of emplacement are higher due to lower temperatures as well as crystal and bubble content, while high water content (present at Fentale; Webster et al., 1993) reduces viscosity especially for peralkaline melts.

Our observations, combined with the Kerr et al. (2006) model, suggest maximum emplacement viscosities of 10^8 – 10^{11} Pa s for peralkaline rhyolite lavas on Fentale (Figure 10), similar to those estimated for calc-alkaline rhyolites (10^{10} – 10^{11} Pa s; e.g., Bagdassarov & Dingwell, 1992; Stevenson et al., 1994). For volumetric flow rates of 1 m³/s or greater, maximum viscosity of the peralkaline rhyolites in this study is $\sim 10^8$ – 10^9 Pa s, consistent with experimental and theoretical approaches in being lower than their calc-alkaline counterparts.

Analysis of the morphology of lava flow deposits using remote sensing data provides valuable constraints on eruptive dynamics. Further investigation of the development of morphological features, in combination with experimental and rheological analyses, may provide important developments in modeling the dynamics of peralkaline lavas.

5. Conclusions

This study provides an abundance of new geomorphological data which, together with geological observations, presents a wealth of information concerning the behavior of several volcanoes in the MER and Afar. Several previously unidentified post-caldera deposits have been observed on Fentale volcano, as well as a number of newly observed craters on Corbetti volcano.

The shapes of calderas in the MER are largely controlled by both rift-parallel and rift-cutting structures. Variations in caldera architecture exist, the caldera at Fentale having a deeper and simpler definition to those at Corbetti and Gedemsa. The more complex caldera shapes may be the result of multiple collapses.

Post-caldera activity at each volcano is aligned with rift-cutting structures in various orientations. Alignment with the rift-parallel faults is also observed, similar to nearby Boset. The influence of the caldera structure on vent location seems less important, in contrast to nearby Aluto. The dominance of faults and other structures controlling the location of vents and craters in the MER and in Afar suggests that the regional stress field, edifice loading, and pressurized reservoirs/conduits play minor roles in determining the location of eruptions.

The relative frequency of eruptions, as discerned from the number of deposits, vents, and craters since caldera formation, varies greatly between volcanoes. Gedemsa has been largely inactive whereas Fentale and Corbetti have produced a number of eruptions in the past 300 kyr. Fentale has produced many small-volume eruptions (<0.1 km³), whereas events at Corbetti are usually much larger (~ 0.4 – 0.5 km³). Basaltic eruptions at large volcanic centers are infrequent in the south of the rift, increasing in frequency to the north.

Typical lava volumes, lengths, and number of vents are reported, providing indicative characteristics for use in hazard planning. Peralkaline rhyolite coulees at Corbetti and Fentale exhibit levees and ogives formed during emplacement. The morphometry of these deposits suggests emplacement viscosities of 10^8 – 10^{11} Pa s compared to 10^{10} – 10^{11} Pa s for calc-alkaline rhyolites—the lower end of our estimates are in

agreement with experimental and theoretical studies suggesting a reduced viscosity for peralkaline melts. Further observations of morphometry and dynamics are required to test this hypothesis, which remains unverified in nature.

Satellite data and remote sensing tools are invaluable resources in rapidly comparing the previous activity of large, inaccessible volcanoes. The observations reported here highlight fundamental questions concerning the dynamics of rift volcanoes, and its variability along rift. Further work regarding the influence of rift structure and peralkaline composition on magma dynamics is needed to progress our understanding of these systems.

Acknowledgments

This work was supported by a studentship from NERC as part of the Environmental Research DTP (University of Oxford) and is a contribution to the Natural Environment Research Council funded RiftVolc project (NE/L013932/1, Rift volcanism: past, present, and future). T.A.M. and D.M.P. are supported by and contribute to the NERC Centre for the Observation and Modelling of Earthquakes, Volcanoes, and Tectonics (COMET). Funding for Pleiades imagery was provided by a grant from COMET. Airborne lidar data for Corbetti were collected during the NERC Airborne Research and Survey Facility (ARSF) campaign ET 12-17, and initial processing was carried out by NERC ARSF Data Analysis Node. Airborne lidar for Dabbahu was acquired by the NERC ARSF and processed at the University of Leeds as part of the Afar Rift Consortium (NE/E007414/1). We thank Fiona Iddon and Abate Assen for field assistance, as well as Karen Fontijn for help in the field and with logistics. We are grateful for the professional logistical support of Ethioder and their drivers. The DEMs in this study are available to download from OpenTopography at the following DOIs: Fentale (10.5069/G9862DKT), Gedemsa (10.5069/G94J0C6X), Urji (10.5069/G9W0941H), Chabbi (10.5069/G90R9MH3), and Dabbahu (10.5069/G9R78C9S, 10.5069/G9MG7MK2). We thank Giacomo Corti and an anonymous reviewer for constructive comments that improved the manuscript.

References

- Abbate, E., & Sagri, M. (1980). Volcanites of the Ethiopian and Somali Plateaus and major tectonic lines. *Accademia Nazionale dei Lincei: Geodynamic Evolution of the Afro-Arabian Rift System: Meeting*, 47, 219–227.
- Abebe, B., Acocella, V., Korme, T., & Ayalew, D. (2007). Quaternary faulting and volcanism in the Main Ethiopian Rift. *Journal of African Earth Sciences*, 48(2–3), 115–124. <https://doi.org/10.1016/j.jafrearsci.2006.10.005>
- Abebe, T., Mazzarini, F., Innocenti, F., & Manetti, P. (1995). The Yerer-Tullu Wellel extensional structure (Central Ethiopia): Evidences from remote sensing, petrologic and geochronologic data. In IEEE (Ed.), *Geoscience and remote sensing symposium, IGARSS'95: "Quantitative Remote Sensing for Science and Applications"*, (Vol. 1, pp. 374–376). Firenze: IEEE. <https://doi.org/10.1109/IGARSS.1995.520285>
- Abebe, T., Mazzarini, F., Innocenti, F., & Manetti, P. (1998). The Yerer-Tullu Wellel volcanotectonic lineament: A transtensional structure in central Ethiopia and the associated magmatic activity. *Journal of African Earth Sciences*, 26(1), 135–150. [https://doi.org/10.1016/S0899-5362\(97\)00141-3](https://doi.org/10.1016/S0899-5362(97)00141-3)
- Acocella, V., Korme, T., Salvini, F., & Funicello, R. (2002). Elliptic calderas in the Ethiopian Rift: Control of pre-existing structures. *Journal of Volcanology and Geothermal Research*, 119(1–4), 189–203. [https://doi.org/10.1016/S0377-0273\(02\)00342-6](https://doi.org/10.1016/S0377-0273(02)00342-6)
- Agostini, A., Bonini, M., Corti, G., Sani, F., & Mazzarini, F. (2011). Fault architecture in the Main Ethiopian Rift and comparison with experimental models: Implications for rift evolution and Nubia-Somalia kinematics. *Earth and Planetary Science Letters*, 301(3–4), 479–492. <https://doi.org/10.1016/j.epsl.2010.11.024>
- Anderson, E. M. (1951). *The dynamics of faulting and dyke formation with applications in Britain*, (2nd ed.). London: Oliver and Boyd.
- Aspinall, W., Auken, M., Hincks, T., Mahony, S., Nadim, F., Pooley, J., et al. (2011). Volcano hazard and exposure in GFDRR priority countries and risk mitigation measures - GFDRR, volcano risk study. Oslo: Bristol University Cabot Institute and Norwegian Geotechnical Institute (NGI) for the World Bank: NGI Report 20100806.
- Bagdassarov, N. S., & Dingwell, D. B. (1992). A rheological investigation of vesicular rhyolite. *Journal of Volcanology and Geothermal Research*, 50(3), 307–322. [https://doi.org/10.1016/0377-0273\(92\)90099-Y](https://doi.org/10.1016/0377-0273(92)90099-Y)
- Bailey, J. E., Harris, A. J. L., Dehn, J., Calvari, S., & Rowland, S. K. (2006). The changing morphology of an open lava channel on Mt. Etna. *Bulletin of Volcanology*, 68(6), 497–515. <https://doi.org/10.1007/s00445-005-0025-6>
- Baloga, S. M., Glaze, L. S., & Bruno, B. C. (2007). Nearest-neighbor analysis of small features on Mars: Applications to tumuli and rootless cones. *Journal of Geophysical Research*, 112, E03002. <https://doi.org/10.1029/2005JE002652>
- Barberi, F., & Varet, J. (1977). Volcanism of Afar: Small-scale plate tectonics implications. *Geological Society of America Bulletin*, 88(9), 1251–1266. [https://doi.org/10.1130/0016-7606\(1977\)88<1251:VOASPT>2.0.CO;2](https://doi.org/10.1130/0016-7606(1977)88<1251:VOASPT>2.0.CO;2)
- Barnie, T. D., Keir, D., Hamling, I., Hofmann, B., Belachew, M., Carn, S., et al. (2016). A multidisciplinary study of the final episode of the Manda Hararo dyke sequence, Ethiopia, and implications for trends in volcanism during the rifting cycle. *Geological Society, London, Special Publications*, 420(1), 149–163. <https://doi.org/10.1144/SP420.6>
- Bellier, O., & Sébrier, M. (1994). Relationship between tectonism and volcanism along the great Sumatran fault zone deduced by spot image analyses. *Tectonophysics*, 233(3–4), 215–231. [https://doi.org/10.1016/0040-1951\(94\)90242-9](https://doi.org/10.1016/0040-1951(94)90242-9)
- Bigazzi, G., Bonadonna, F., Di Paola, G. M., & Giuliani, O. (1993). K-Ar and fission track ages of the last volcano tectonic phase in the Ethiopian Rift Valley (Tullu Moye Area). In *Geology and mineral resources of Somalia and surrounding regions, Relazioni e monografie agrarie subtropicali e tropicali*, (Vol. 113, pp. 311–322). Firenze: Istituto Agronomico per l'Oltremare.
- Biggs, J., Bastow, I. D., Keir, D., & Lewi, E. (2011). Pulses of deformation reveal frequently recurring shallow magmatic activity beneath the Main Ethiopian Rift. *Geochemistry, Geophysics, Geosystems*, 12, Q0AB10. <https://doi.org/10.1029/2011GC003662>
- Casey, M., Ebinger, C., Keir, D., Gloaguen, R., & Mohamed, F. (2006). Strain accommodation in transitional rifts: Extension by magma intrusion and faulting in Ethiopian rift magmatic segments. *Geological Society, London, Special Publications*, 259(1), 143–163. <https://doi.org/10.1144/GSL.SP.2006.259.01.13>
- Cashman, K. V., Soule, S. A., Mackey, B. H., Deligne, N. I., Deardorff, N. D., & Dietterich, H. R. (2013). How lava flows: New insights from applications of lidar technologies to lava flow studies. *Geosphere*, 9(6), 1664–1680. <https://doi.org/10.1130/GES00706.1>
- Castruccio, A., Rust, A. C., & Sparks, R. S. J. (2013). Evolution of crust- and core-dominated lava flows using scaling analysis. *Bulletin of Volcanology*, 75(1), 1–15. <https://doi.org/10.1007/s00445-012-0681-2>
- Córdoba, G., Villarosa, G., Sheridan, M. F., Viramonte, J. G., Beigt, D., & Salmuni, G. (2015). Secondary lahar hazard assessment for Villa la Angostura, Argentina, using two-phase-titan modelling code during 2011 Cordón Caulle eruption. *Natural Hazards and Earth System Sciences*, 15(4), 757–766. <https://doi.org/10.5194/nhess-15-757-2015>
- Corti, G. (2009). Continental rift evolution: From rift initiation to incipient break-up in the Main Ethiopian Rift, East Africa. *Earth-Science Reviews*, 96(1–2), 1–53. <https://doi.org/10.1016/j.earscirev.2009.06.005>
- Corti, G., Molin, P., Sembroni, A., Bastow, I. D., & Keir, D. (2018). Control of pre-rift lithospheric structure on the architecture and evolution of continental rifts: Insights from the Main Ethiopian Rift, East Africa. *Tectonics*, 37, 477–496. <https://doi.org/10.1002/2017TC004799>
- Corti, G., Sani, F., Agostini, S., Philippon, M., Sokoutis, D., & Willingshofer, E. (2018). Off-axis volcano-tectonic activity during continental rifting: Insights from the transversal Goba-Gonga lineament, Main Ethiopian Rift (East Africa). *Tectonophysics*, 728–729(August 2017), 75–91. <https://doi.org/10.1016/j.tecto.2018.02.011>
- Corti, G., Sani, F., Philippon, M., Sokoutis, D., Willingshofer, E., & Molin, P. (2013). Quaternary volcano-tectonic activity in the Soddo region, western margin of the southern Main Ethiopian Rift. *Tectonics*, 32, 861–879. <https://doi.org/10.1002/tect.20052>

- Csatho, B., Schenk, T., Kyle, P., Wilson, T., & Krabill, W. B. (2008). Airborne laser swath mapping of the summit of Erebus volcano, Antarctica: Applications to geological mapping of a volcano. *Journal of Volcanology and Geothermal Research*, 177(3), 531–548. <https://doi.org/10.1016/j.jvolgeores.2008.08.016>
- Deardorff, N. D., & Cashman, K. V. (2012). Emplacement conditions of the c. 1,600-year bp Collier Cone lava flow, Oregon: A LiDAR investigation. *Bulletin of Volcanology*, 74(9), 2051–2066. <https://doi.org/10.1007/s00445-012-0650-9>
- Di Genova, D., Romano, C., Hess, K. U., Vona, A., Poe, B. T., Giordano, D., et al. (2013). The rheology of peralkaline rhyolites from Pantelleria Island. *Journal of Volcanology and Geothermal Research*, 249, 201–216. <https://doi.org/10.1016/j.jvolgeores.2012.10.017>
- Di Paola, G. M. (1971). Geology of the Corbetti Caldera area (Main Ethiopian Rift Valley). *Bulletin Volcanologique*, 35(2), 497–506. <https://doi.org/10.1007/BF02596970>
- Dingwell, D. B., Hess, K. U., & Romano, C. (1998). Extremely fluid behavior of hydrous peralkaline rhyolites. *Earth and Planetary Science Letters*, 158(1–2), 31–38. [https://doi.org/10.1016/S0012-821X\(98\)00046-6](https://doi.org/10.1016/S0012-821X(98)00046-6)
- Donovan, A., Blundy, J., Oppenheimer, C., & Buisman, I. (2018). The 2011 eruption of Nabro volcano, Eritrea: Perspectives on magmatic processes from melt inclusions. *Contributions to Mineralogy and Petrology*, 173(1), 1. <https://doi.org/10.1007/s00410-017-1425-2>
- Ernst, G. G. J., Kervyn, M., & Teeuw, R. M. (2008). Advances in the remote sensing of volcanic activity and hazards, with special consideration to applications in developing countries. *International Journal of Remote Sensing*, 29(22), 6687–6723. <https://doi.org/10.1080/01431160802168459>
- Euillades, L. D., Grosse, P., & Euillades, P. A. (2013). NETVOLC: An algorithm for automatic delimitation of volcano edifice boundaries using DEMs. *Computers and Geosciences*, 56, 151–160. <https://doi.org/10.1016/j.cageo.2013.03.011>
- Fagents, S. A., & Thordarson, T. (2007). Rootless volcanic cones in Iceland and on Mars. In *The geology of Mars: Evidence from Earth-based analogs*, (pp. 151–177). Cambridge: Cambridge Univ. Press. <https://doi.org/10.1017/cbo9780511536014.007>
- Favalli, M., & Fornaciai, A. (2017). Visualization and comparison of DEM-derived parameters. Application to volcanic areas. *Geomorphology*, 290, 69–84. <https://doi.org/10.1016/j.geomorph.2017.02.029>
- Favalli, M., Innocenti, F., Pareschi, M. T., Pasquarè, G., Mazzarini, F., Branca, S., et al. (1999). The DEM of Mount Etna: Geomorphological and structural implications. *Geodinamica Acta*, 12(5), 279–290. <https://doi.org/10.1080/09853111.1999.11105350>
- Favalli, M., Pareschi, M. T., Neri, A., & Isola, I. (2005). Forecasting lava flow paths by a stochastic approach. *Geophysical Research Letters*, 32, L03305. <https://doi.org/10.1029/2004GL021718>
- Ferguson, D. J., Barnie, T. D., Pyle, D. M., Oppenheimer, C., Yirgu, G., Lewi, E., et al. (2010). Recent rift-related volcanism in Afar, Ethiopia. *Earth and Planetary Science Letters*, 292(3–4), 409–418. <https://doi.org/10.1016/j.epsl.2010.02.010>
- Field, L., Blundy, J., Brooker, R. A., Wright, T., & Yirgu, G. (2012). Magma storage conditions beneath Dabbahu Volcano (Ethiopia) constrained by petrology, seismicity and satellite geodesy. *Bulletin of Volcanology*, 74(5), 981–1004. <https://doi.org/10.1007/s00445-012-0580-6>
- Field, L., Blundy, J., Calvert, A., & Yirgu, G. (2013). Magmatic history of Dabbahu, a composite volcano in the Afar Rift, Ethiopia. *Bulletin of the Geological Society of America*, 125(1–2), 128–147. <https://doi.org/10.1130/B30560.1>
- Fink, J. (1980). Surface folding and viscosity of rhyolite flows. *Geology*, 8(5), 250–254. [https://doi.org/10.1130/0091-7613\(1980\)8<250:SFAVOR>2.0.CO;2](https://doi.org/10.1130/0091-7613(1980)8<250:SFAVOR>2.0.CO;2)
- Fink, J. H., & Fletcher, R. C. (1978). Ropy pahoehoe: Surface folding of a viscous fluid. *Journal of Volcanology and Geothermal Research*, 4(1–2), 151–170. [https://doi.org/10.1016/0377-0273\(78\)90034-3](https://doi.org/10.1016/0377-0273(78)90034-3)
- Fink, J. H., & Griffiths, R. W. (1990). Radial spreading of viscous gravity currents with solidifying crust. *Journal of Fluid Mechanics*, 221, 485–509. <https://doi.org/10.1017/S0022112090003640>
- Fink, J. H., & Griffiths, R. W. (1998). Morphology, eruption rates, and rheology of lava domes: Insights from laboratory models. *Journal of Geophysical Research*, 103(B1), 527–545. <https://doi.org/10.1029/97JB02838>
- Fontijn, K., McNamara, K., Zafu Tadesse, A., Pyle, D. M., Dessalegn, F., Hutchison, W., et al. (2018). Contrasting styles of post-caldera volcanism along the Main Ethiopian Rift: Implications for contemporary volcanic hazards. *Journal of Volcanology and Geothermal Research*, 356, 90–113. <https://doi.org/10.1016/j.jvolgeores.2018.02.001>
- Fornaciai, A., Favalli, M., Karátson, D., Tarquini, S., & Boschi, E. (2012). Morphometry of scoria cones, and their relation to geodynamic setting: A DEM-based analysis. *Journal of Volcanology and Geothermal Research*, 217–218, 56–72. <https://doi.org/10.1016/j.jvolgeores.2011.12.012>
- Gibson, I. L. (1967). Preliminary account of the volcanic geology of Fantale, Shoa. *Bulletin of the Geophysical Observatory of Addis Ababa*, 10, 59–67.
- Gibson, I. L. (1969). The structure and volcanic geology of an axial portion of the Main Ethiopian Rift. *Tectonophysics*, 8(4–6), 561–565. [https://doi.org/10.1016/0040-1951\(69\)90054-7](https://doi.org/10.1016/0040-1951(69)90054-7)
- Gibson, I. L. (1970). A Pantelleritic welded ash-flow tuff flow from the Ethiopian Rift Valley. *Contributions to Mineralogy and Petrology*, 28(2), 89–111. <https://doi.org/10.1007/BF00404992>
- Gibson, I. L. (1972). The chemistry and petrogenesis of a suite of pantellerites from the Ethiopian Rift. *Journal of Petrology*, 13(1), 31–44. <https://doi.org/10.1093/petrology/13.1.31>
- Gibson, I. L. (1974). A review of the geology, petrology and geochemistry of the volcano Fantale. *Bulletin Volcanologique*, 38(2), 791–802. <https://doi.org/10.1007/BF02596908>
- Giordano, D., Russell, J. K., & Dingwell, D. B. (2008). Viscosity of magmatic liquids: A model. *Earth and Planetary Science Letters*, 271(1–4), 123–134. <https://doi.org/10.1016/j.epsl.2008.03.038>
- Giordano, F., D'Antonio, M., Civetta, L., Tonarini, S., Orsi, G., Ayalew, D., et al. (2014). Genesis and evolution of mafic and felsic magmas at Quaternary volcanoes within the Main Ethiopian Rift: Insights from Gedemsa and Fanta'Ale complexes. *Lithos*, 188, 130–144. <https://doi.org/10.1016/j.lithos.2013.08.008>
- Gislason, G., H. Eysteinnsson, G. Björnsson, & V. Harðardóttir (2015). Results of surface exploration in the Corbetti Geothermal Area, Ethiopia. In *Proceedings of the World Geothermal Congress, 2015*. Melbourne, Australia.
- Gleeson, M. L. M., Stock, M. J., Pyle, D. M., Mather, T. A., Hutchison, W., Yirgu, G., & Wade, J. (2017). Constraining magma storage conditions at a restless volcano in the Main Ethiopian Rift using phase equilibria models. *Journal of Volcanology and Geothermal Research*, 337, 44–61. <https://doi.org/10.1016/j.jvolgeores.2017.02.026>
- Gregg, T. K. P. (2017). Patterns and processes: Subaerial lava flow morphologies: A review. *Journal of Volcanology and Geothermal Research*, 342, 3–12. <https://doi.org/10.1016/j.jvolgeores.2017.04.022>
- Gregg, T. K. P., & Fink, J. H. (2000). A laboratory investigation into the effects of slope on lava flow morphology. *Journal of Volcanology and Geothermal Research*, 96(3–4), 145–159. [https://doi.org/10.1016/S0377-0273\(99\)00148-1](https://doi.org/10.1016/S0377-0273(99)00148-1)
- Gregg, T. K. P., Fink, J. H., & Griffiths, R. W. (1998). Formation of multiple fold generations on lava flow surfaces: Influence of strain rate, cooling rate, and lava composition. *Journal of Volcanology and Geothermal Research*, 80(3–4), 281–292. [https://doi.org/10.1016/S0377-0273\(97\)00048-6](https://doi.org/10.1016/S0377-0273(97)00048-6)

- Grosse, P., Euillades, P. A., Euillades, L. D., & van Wyk de Vries, B. (2014). A global database of composite volcano morphometry. *Bulletin of Volcanology*, 76(1), 1–16. <https://doi.org/10.1007/s00445-013-0784-4>
- Guðmundsson, Á. (1995). Infrastructure and mechanics of volcanic systems in Iceland. *Journal of Volcanology and Geothermal Research*, 64(1–2), 1–22. [https://doi.org/10.1016/0377-0273\(95\)92782-Q](https://doi.org/10.1016/0377-0273(95)92782-Q)
- Harris, W. C. (1844). *The highlands of Ethiopia*, (2nd ed.). London: Longman, Brown, Green, and Longmans. <https://doi.org/10.5479/sil.211328.39088000130062>
- Hayward, N. J., & Ebinger, C. J. (1996). Variations in the along-axis segmentation of the Afar Rift system. *Tectonics*, 15(2), 244–257. <https://doi.org/10.1029/95TC02292>
- Hess, K. U., Dingwell, D. B., & Webb, S. L. (1995). The influence of excess alkalis on the viscosity of a haplogranitic melt. *American Mineralogist*, 80(3–4), 297–304. <https://doi.org/10.2138/am-1995-3-411>
- Hofmann, B. (2013). How do faults grow in magmatic rifts? LiDAR and InSAR observations of the Dabbahu rift segment, Afar, Ethiopia. PhD Thesis, University of Leeds.
- Hofman, M. A., Malavassi, E., & Blair, J. B. (2006). Quantifying recent pyroclastic and lava flows at Arenal Volcano, Costa Rica, using medium-footprint lidar. *Geophysical Research Letters*, 33, L21306. <https://doi.org/10.1029/2006GL027822>
- Holohan, E. P., Troll, V. R., Walter, T. R., Münn, S., McDonnell, S., & Shipton, Z. K. (2005). Elliptical calderas in active tectonic settings: An experimental approach. *Journal of Volcanology and Geothermal Research*, 144, 119–136. <https://doi.org/10.1016/j.jvolgeores.2004.11.020>
- Hughes, E. C., Neave, D. A., Dobson, K. J., Withers, P. J., & Edmonds, M. (2017). How to fragment peralkaline rhyolites: Observations on pumice using combined multi-scale 2D and 3D imaging. *Journal of Volcanology and Geothermal Research*, 336, 179–191. <https://doi.org/10.1016/j.jvolgeores.2017.02.020>
- Hulme, G. (1974). The interpretation of lava flow morphology. *Geophysical Journal International*, 39(2), 361–383. <https://doi.org/10.1111/j.1365-246X.1974.tb05460.x>
- Hutchison, W., Biggs, J., Mather, T. A., Pyle, D. M., Lewi, E., Yirgu, G., et al. (2016). Causes of unrest at silicic calderas in the east African Rift: New constraints from InSAR and soil-gas chemistry at Aluto volcano, Ethiopia. *Geochemistry, Geophysics, Geosystems*, 17, 3008–3030. <https://doi.org/10.1002/2016GC006395>
- Hutchison, W., Fusillo, R., Pyle, D. M., Mather, T. A., Blundy, J. D., Biggs, J., et al. (2016). A pulse of mid-Pleistocene rift volcanism in Ethiopia at the dawn of modern humans. *Nature Communications*, 7, 13192. <https://doi.org/10.1038/ncomms13192>
- Hutchison, W., Mather, T. A., Pyle, D. M., Biggs, J., & Yirgu, G. (2015). Structural controls on fluid pathways in an active rift system: A case study of the Aluto volcanic complex. *Geosphere*, 11(3), 542–562. <https://doi.org/10.1130/GES01119.1>
- Hutchison, W., Mather, T. A., Pyle, D. M., Boyce, A. J., Gleeson, M. L. M., Yirgu, G., et al. (2018). The evolution of magma during continental rifting: New constraints from the isotopic and trace element signatures of silicic magmas from Ethiopian volcanoes. *Earth and Planetary Science Letters*, 489, 203–218. <https://doi.org/10.1016/j.epsl.2018.02.027>
- Hutchison, W., Pyle, D. M., Mather, T. A., Yirgu, G., Biggs, J., Cohen, B. E., et al. (2016). The eruptive history and magmatic evolution of Aluto volcano: New insights into silicic peralkaline volcanism in the Ethiopian Rift. *Journal of Volcanology and Geothermal Research*, 328, 9–33. <https://doi.org/10.1016/j.jvolgeores.2016.09.010>
- Jeffery, A. J., Gertisser, R., O'Driscoll, B., Pacheco, J. M., Whitley, S., Pimentel, A., & Self, S. (2016). Temporal evolution of a post-caldera, mildly peralkaline magmatic system: Furnas volcano, São Miguel, Azores. *Contributions to Mineralogy and Petrology*, 171(5), 1–24. <https://doi.org/10.1007/s00410-016-1235-y>
- Jessop, D. E., Kelfoun, K., Labazuy, P., Mangeney, A., Roche, O., Tillier, J. L., et al. (2012). LiDAR derived morphology of the 1993 Lascar pyroclastic flow deposits, and implication for flow dynamics and rheology. *Journal of Volcanology and Geothermal Research*, 245–246, 81–97. <https://doi.org/10.1016/j.jvolgeores.2012.06.030>
- Keir, D., Bastow, I. D., Corti, G., Mazzarini, F., & Rooney, T. O. (2015). The origin of along-rift variations in faulting and magmatism in the Ethiopian Rift. *Tectonics*, 34, 464–477. <https://doi.org/10.1002/2014TC003698>
- Keir, D., Bastow, I. D., Pagli, C., & Chambers, E. L. (2013). The development of extension and magmatism in the Red Sea Rift of Afar. *Tectonophysics*, 607, 98–114. <https://doi.org/10.1016/j.tecto.2012.10.015>
- Keir, D., Hamling, I. J., Ayele, A., Calais, E., Ebinger, C., Wright, T. J., et al. (2009). Evidence for focused magmatic accretion at segment centers from lateral dike injections captured beneath the Red Sea Rift in Afar. *Geology*, 37(1), 59–62. <https://doi.org/10.1130/G25147A.1>
- Kerr, R. C., Griffiths, R. W., & Cashman, K. V. (2006). Formation of channelized lava flows on an unconfined slope. *Journal of Geophysical Research*, 111, B10206. <https://doi.org/10.1029/2005JB004225>
- Kervyn, M., Ernst, G. G. J., Carracedo, J. C., & Jacobs, P. (2012). Geomorphometric variability of “monogenetic” volcanic cones: Evidence from Mauna Kea, Lanzarote and experimental cones. *Geomorphology*, 136(1), 59–75. <https://doi.org/10.1016/j.geomorph.2011.04.009>
- Kervyn, M., Kervyn, F., Goossens, R., Rowland, S. K., & Ernst, G. G. J. (2007). Mapping volcanic terrain using high-resolution and 3D satellite remote sensing. *Geological Society, London, Special Publications*, 283(1), 5–30. <https://doi.org/10.1144/SP283.2>
- Latutrie, B., Harris, A., Médard, E., & Gurioli, L. (2017). Eruption and emplacement dynamics of a thick trachytic lava flow of the Sancy volcano (France). *Bulletin of Volcanology*, 79(1), 1–21. <https://doi.org/10.1007/s00445-016-1084-6>
- Lescinsky, D. T., Skoblenick, S. V., & Mansinha, L. (2007). Automated identification of lava flow structures using local Fourier spectrum of digital elevation data. *Journal of Geophysical Research*, 112, B05212. <https://doi.org/10.1029/2006JB004263>
- Lloyd, R., Biggs, J., Birhanu, Y., Wilks, M., Kendall, J., Ayele, A., & Lewi, E. (2018). Sustained uplift at a continental rift Caldera. *Journal of Geophysical Research: Solid Earth*, 123, 5209–5226. <https://doi.org/10.1029/2018JB015711>
- Lloyd, R., Biggs, J., Wilks, M., Nowacki, A., Kendall, J. M., Ayele, A., et al. (2018). Evidence for cross rift structural controls on deformation and seismicity at a continental rift caldera. *Earth and Planetary Science Letters*, 487, 190–200. <https://doi.org/10.1016/j.epsl.2018.01.037>
- Macdonald, R., & Gibson, I. L. (1969). Pantelleritic obsidians from the volcano Chabbi (Ethiopia). *Contributions to Mineralogy and Petrology*, 24(3), 239–244. <https://doi.org/10.1007/BF00376050>
- Mahood, G. A. (1984). Pyroclastic rocks and calderas associated with strongly peralkaline magmatism. *Journal of Geophysical Research*, 89(B10), 8540–8552. <https://doi.org/10.1029/JB089iB10p08540>
- Mahood, G. A., & Hildreth, W. (1986). Geology of the peralkaline volcano at Pantelleria, Strait of Sicily. *Bulletin of Volcanology*, 48(2–3), 143–172. <https://doi.org/10.1007/BF01046548>
- Martin-Jones, C. M., Lane, C. S., Pearce, N. J. G., Smith, V. C., Lamb, H. F., Schaebitz, F., et al. (2017). Recurrent explosive eruptions from a high-risk Main Ethiopian Rift volcano throughout the Holocene. *Geology*, 45(12), 1127–1130. <https://doi.org/10.1130/G39594.1>
- Mazzarini, F., Pareschi, M. T., Favalli, M., Isola, I., Tarquini, S., & Boschi, E. (2005). Morphology of basaltic lava channels during the Mt. Etna September 2004 eruption from airborne laser altimeter data. *Geophysical Research Letters*, 32, L04305. <https://doi.org/10.1029/2004GL021815>

- McNamara, K., Cashman, K. V., Rust, A. C., Fontijn, K., Chalié, F., Tomlinson, E. L., & Yirgu, G. (2018). Using Lake sediment cores to improve records of volcanism at Aluto volcano in the Main Ethiopian Rift. *Geochemistry, Geophysics, Geosystems*, 19, 3164–3188. <https://doi.org/10.1029/2018GC007686>
- Medynski, S., Pik, R., Burnard, P., Williams, A., Vye-Brown, C., Ferguson, D., et al. (2013). Controls on magmatic cycles and development of rift topography of the Manda Hararo segment (Afar, Ethiopia): Insights from cosmogenic ³He investigation of landscape evolution. *Earth and Planetary Science Letters*, 367, 133–145. <https://doi.org/10.1016/j.epsl.2013.02.006>
- Mohr, P. A. (1966). Chabbi Volcano (Ethiopia). *Bulletin Volcanologique*, 29(1), 797–815. <https://doi.org/10.1007/BF02597195>
- Moore, H. J., Arthur, D. W. G., & Schaber, G. G. (1978). Yield strengths of flows on the Earth, Mars, and Moon. In *Proceedings of the Ninth Lunar and Planetary Scientific Conference (Vol. 3)* (pp. 3351–3378). Houston, Texas.
- Muirhead, J. D., Kattenhorn, S. A., & Le Corvec, N. (2015). Varying styles of magmatic strain accomodation across the east African Rift. *Geochemistry, Geophysics, Geosystems*, 16, 2775–2795. <https://doi.org/10.1002/2015GC005918>
- Nakamura, K. (1977). Volcanoes as possible indicators of tectonic stress orientation - principle and proposal. *Journal of Volcanology and Geothermal Research*, 98, 401–416. <https://doi.org/10.1007/BF02199968>
- Nomikou, P., Parks, M. M., Papanikolaou, D., Pyle, D. M., Mather, T. A., Carey, S., et al. (2014). The emergence and growth of a submarine volcano: The Kameni islands, Santorini (Greece). *GeoResJ*, 1–2, 8–18. <https://doi.org/10.1016/j.grj.2014.02.002>
- Nowacki, A., Wilks, M., Kendall, J. M., Biggs, J., & Ayele, A. (2018). Characterising hydrothermal fluid pathways beneath Aluto volcano, Main Ethiopian Rift, using shear wave splitting. *Journal of Volcanology and Geothermal Research*, 356, 331–341. <https://doi.org/10.1016/j.jvolgeores.2018.03.023>
- Peccerillo, A., Barberio, M. R., Yirgu, G., Ayalew, D., Barbieri, M., & Wu, T. W. (2003). Relationships between mafic and peralkaline silicic magmatism in continental rift settings: A petrological, geochemical and isotopic study of the Gedemsa Volcano, central Ethiopian Rift. *Journal of Petrology*, 44(11), 2003–2032. <https://doi.org/10.1093/petrology/egg068>
- Peccerillo, A., Donati, C., Santo, A. P., Orlando, A., Yirgu, G., & Ayalew, D. (2007). Petrogenesis of silicic peralkaline rocks in the Ethiopian Rift: Geochemical evidence and volcanological implications. *Journal of African Earth Sciences*, 48(2–3), 161–173. <https://doi.org/10.1016/j.jafrearsci.2006.06.010>
- Pedersen, G. B. M., & Grosse, P. (2014). Morphometry of subaerial shield volcanoes and glaciovolcanoes from Reykjanes Peninsula, Iceland: Effects of eruption environment. *Journal of Volcanology and Geothermal Research*, 282, 115–133. <https://doi.org/10.1016/j.jvolgeores.2014.06.008>
- Peitersen, M. N., & Crown, D. A. (1999). Downflow width behavior of Martian and terrestrial lava flows. *Journal of Geophysical Research*, 104(E4), 8473–8488. <https://doi.org/10.1029/1999JE900003>
- Prima, O. D. A., & Yoshida, T. (2010). Characterization of volcanic geomorphology and geology by slope and topographic openness. *Geomorphology*, 118(1–2), 22–32. <https://doi.org/10.1016/j.geomorph.2009.12.005>
- Pyle, D. M., & Elliott, J. R. (2006). Quantitative morphology, recent evolution, and future activity of the Kameni Islands volcano, Santorini, Greece. *Geosphere*, 2(5), 253–268. <https://doi.org/10.1130/GES00028.1>
- Ramsey, M. L., Oppenheimer, C., Pyle, D. M., & Yirgu, G. (2010). Caldera-forming eruptions of the Quaternary Kone volcanic complex, Ethiopia. *Journal of African Earth Sciences*, 58(1), 51–66. <https://doi.org/10.1016/j.jafrearsci.2010.01.008>
- Rapprich, V., Žáček, V., Verner, K., Erban, V., Goslar, T., Bekele, Y., et al. (2016). Wendo Koshe Pumice: The latest Holocene silicic explosive eruption product of the Corbetti volcanic system (southern Ethiopia). *Journal of Volcanology and Geothermal Research*, 310, 159–171. <https://doi.org/10.1016/j.jvolgeores.2015.12.008>
- Robertson, E. A. M., Biggs, J., Cashman, K. V., Floyd, M. A., & Vye-Brown, C. (2015). Influence of regional tectonics and pre-existing structures on the formation of elliptical calderas in the Kenyan Rift. *Geological Society, London, Special Publications*, 420(1), 43–67. <https://doi.org/10.1144/SP420.12>
- Rogers, P. G., M. T. Zuber, & B. A. Campbell (1996). Crossflow topographic effects on the emplacement of leveed lava flows: Implications for Venusian lava flows. In *Lunar and Planetary Science Conference (Vol. XXVII, pp. 1095–1096)*.
- Romine, W. L., Whittington, A. G., Nabelek, P. I., & Hofmeister, A. M. (2012). Thermal diffusivity of rhyolitic glasses and melts: Effects of temperature, crystals and dissolved water. *Bulletin of Volcanology*, 74(10), 2273–2287. <https://doi.org/10.1007/s00445-012-0661-6>
- Samrock, F., Kuvshinov, A., Bakker, J., Jackson, A., & Fisseha, S. (2015). 3-D analysis and interpretation of magnetotelluric data from the Aluto-Langano geothermal field, Ethiopia. *Geophysical Journal International*, 202(3), 1923–1948. <https://doi.org/10.1093/gji/ggv270>
- Saria, E., Calais, E., Stamps, D. S., Delvaux, D., & Hartnady, C. J. H. (2014). Present-day kinematics of the east African Rift. *Journal of Geophysical Research: Solid Earth*, 119, 3584–3600. <https://doi.org/10.1002/2013JB010901>
- Sieburg, M., Gernon, T. M., Bull, J. M., Keir, D., Barfod, D. N., Taylor, R. N., et al. (2017). Geological evolution of the Boset-Bericha volcanic complex, Main Ethiopian Rift: ⁴⁰Ar/³⁹Ar evidence for episodic Pleistocene to Holocene volcanism. *Journal of Volcanology and Geothermal Research*, 351, 115–133. <https://doi.org/10.1016/j.jvolgeores.2017.12.014>
- Sparks, R. S. J., Pinkerton, H., & Hulme, G. (1976). Classification and formation of lava levees on Mount Etna, Sicily. *Geology*, 4(5), 269–271. [https://doi.org/10.1130/0091-7613\(1976\)4<269:CAFOLL>2.0.CO;2](https://doi.org/10.1130/0091-7613(1976)4<269:CAFOLL>2.0.CO;2)
- Spinks, K. D., Acocella, V., Cole, J. W., & Bassett, K. N. (2005). Structural control of volcanism and caldera development in the transtensional Taupo volcanic zone, New Zealand. *Journal of Volcanology and Geothermal Research*, 144, 7–22. <https://doi.org/10.1016/j.jvolgeores.2004.11.014>
- Stefanescu, E. R., Bursik, M., & Patra, A. K. (2012). Effect of digital elevation model on Mohr-Coulomb geophysical flow model output. *Natural Hazards*, 62(2), 635–656. <https://doi.org/10.1007/s11069-012-0103-y>
- Stevenson, R. J., Hodder, A. P. W., & Briggs, R. M. (1994). Rheological estimates of rhyolite lava flows from the Okataina Volcanic Centre, New Zealand. *New Zealand Journal of Geology and Geophysics*, 37(2), 211–221. <https://doi.org/10.1080/00288306.1994.9514616>
- Tadesse, A. Z., Ayalew, D., Pik, R., Yirgu, G., & Fontijn, K. (2018). Magmatic evolution of the Boku Volcanic Complex, Main Ethiopian Rift. *Journal of African Earth Sciences*, 149, 109–130. <https://doi.org/10.1016/j.jafrearsci.2018.08.003>
- Tarquini, S., Favalli, M., Mazzarini, F., Isola, I., & Fornaciai, A. (2012). Morphometric analysis of lava flow units: Case study over LIDAR-derived topography at Mount Etna, Italy. *Journal of Volcanology and Geothermal Research*, 235–236, 11–22. <https://doi.org/10.1016/j.jvolgeores.2012.04.026>
- Thouret, J. C. (1999). Volcanic geomorphology—An overview. *Earth Science Reviews*, 47(1–2), 95–131. [https://doi.org/10.1016/S0012-8252\(99\)00014-8](https://doi.org/10.1016/S0012-8252(99)00014-8)
- Thrall, R. (1973). *Gadamsa Caldera, Ethiopia*. Center for Astrophysics, Harvard College Observatory and Smithsonian Astrophysical Observatory (Preprint Series No. 280).
- Ventura, G., & Vilardo, G. (2007). Emplacement mechanism of gravity flows inferred from high resolution Lidar data: The 1944 Somma-Vesuvius lava flow (Italy). *Geomorphology*, 95, 223–235. <https://doi.org/10.1016/j.geomorph.2007.06.005>

- Vye-Brown, C., Sparks, R. S. J., Lewi, E., Mewa, G., Asrat, A., Loughlin, S. C., et al. (2016). Ethiopian volcanic hazards: A changing research landscape. *Geological Society, London, Special Publications*, 420(1), 355–365. <https://doi.org/10.1144/SP420.16>
- Wadge, G., Biggs, J., Lloyd, R., & Kendall, J.-M. (2016). Historical volcanism and the state of stress in the east African Rift System. *Frontiers in Earth Science*, 4. <https://doi.org/10.3389/feart.2016.00086>
- Wadge, G., & Lopes, R. M. C. (1991). The lobes of lava flows on Earth and Olympus Mons, Mars. *Bulletin of Volcanology*, 54(1), 10–24. <https://doi.org/10.1007/BF00278203>
- Wantim, M. N., Kervyn, M., Ernst, G. G. J., Marmol, M. A., Suh, C. E., & Jacobs, P. (2013). Numerical experiments on the dynamics of channelised lava flows at Mount Cameroon volcano with the FLOWGO thermo-rheological model. *Journal of Volcanology and Geothermal Research*, 253, 35–53. <https://doi.org/10.1016/j.jvolgeores.2012.12.003>
- Warner, N. H., & Gregg, T. K. P. (2003). Evolved lavas on Mars? Observations from southwest Arsia Mons and Sabancaya volcano, Peru. *Journal of Geophysical Research*, 108(E10), 5112. <https://doi.org/10.1029/2002JE001969>
- Webster, J. D., Taylor, R. P., & Bean, C. (1993). Pre-eruptive melt composition and constraints on degassing of a water-rich pantellerite magma, Fantale volcano, Ethiopia. *Contributions to Mineralogy and Petrology*, 114(1), 53–62. <https://doi.org/10.1007/BF00307865>
- Wilks, M., Kendall, J.-M., Nowacki, A., Biggs, J., Wookey, J., Birhanu, Y., et al. (2017). Seismicity associated with magmatism, faulting and geothermal circulation at Aluto volcano, Main Ethiopian Rift. *Journal of Volcanology and Geothermal Research*, 340, 52–67. <https://doi.org/10.1016/j.jvolgeores.2017.04.003>
- Williams, F. M., Williams, M. A. J., & Aumento, F. (2004). Tensional fissures and crustal extension rates in the northern part of the Main Ethiopian Rift. *Journal of African Earth Sciences*, 38(2), 183–197. <https://doi.org/10.1016/j.jafrearsci.2003.10.007>
- Wilson, L., & Mouginiis-Mark, P. J. (2014). Dynamics of a fluid flow on Mars: Lava or mud? *Icarus*, 233, 268–280. <https://doi.org/10.1016/j.icarus.2014.01.041>
- Wolfenden, E., Ebinger, C., Yirgu, G., Deino, A., & Ayalew, D. (2004). Evolution of the northern Main Ethiopian Rift: Birth of a triple junction. *Earth and Planetary Science Letters*, 224(1–2), 213–228. <https://doi.org/10.1016/j.epsl.2004.04.022>
- Wolfenden, E., Ebinger, C., Yirgu, G., Renne, P. R., & Kelley, S. P. (2005). Evolution of a volcanic rifted margin: Southern Red Sea, Ethiopia. *Bulletin of the Geological Society of America*, 117(7), 846–864. <https://doi.org/10.1130/B25516.1>
- Wright, T. J., Ebinger, C., Biggs, J., Ayele, A., Yirgu, G., Keir, D., & Stork, A. (2006). Magma-maintained rift segmentation at continental rupture in the 2005 Afar dyking episode. *Nature*, 442(7100), 291–294. <https://doi.org/10.1038/nature04978>
- Wright, T. J., Sigmundsson, F., Pagli, C., Belachew, M., Hamling, I. J., Brandsdóttir, B., et al. (2012). Geophysical constraints on the dynamics of spreading centres from rifting episodes on land. *Nature Geoscience*, 5(4), 242–250. <https://doi.org/10.1038/NGEO1428>
- Žáček, V., V. Rappich, Y. Aman, B. Berhanu, D. Čížek, K. Dereje, et al. (2014). Explanation booklet to the set of geoscience maps of Ethiopia at scale 1:50,000, subsheet 0738-C4 Hawasa. Prague/Addis Ababa, Czech Republic/Ethiopia: Czech Geological Survey/Aquatest/Geological Survey of Ethiopia.
- Žáček, V., Rappich, V., Šíma, J., Škoda, R., Laufek, F., & Legesa, F. (2015). Kogarkoite, Na₃(SO₄)F, from the shalo hot spring, Main Ethiopian Rift: Implications for F-enrichment of thermal groundwater related to alkaline silicic volcanic rocks. *Journal of Geosciences (Czech Republic)*, 60(3), 171–179. <https://doi.org/10.3190/jgeosci.195>
- Zhou, Y., Parsons, B., Elliott, J. R., Barisin, I., & Walker, R. T. (2015). Assessing the ability of Pleiades stereo imagery to determine height changes in earthquakes: A case study for the El Mayor-Cucapah epicentral area. *Journal of Geophysical Research: Solid Earth*, 120, 8793–8808. <https://doi.org/10.1002/2015JB012358>
- Zouzias, D., Miliareisis, G. C., & Seymour, K. S. (2011). Interpretation of Nisyros volcanic terrain using land surface parameters generated from the ASTER Global Digital Elevation Model. *Journal of Volcanology and Geothermal Research*, 200(3–4), 159–170. <https://doi.org/10.1016/j.jvolgeores.2010.12.012>